Supplementary Information

Alloying as a Strategy to Boost the Stability of Copper Nanocatalysts during the Electrochemical CO$_2$ Reduction Reaction.

Valery Okatenko, Anna Loiudice, Mark A. Newton, Dragos C. Stoian, Anastasia Blokhina, Alexander N. Chen, Kevin Rossi, Raffaella Buonsanti*

*email: raffaella.buonsanti@epfl.ch

METHODS

Materials characterization

Selected area electron diffraction (SAED) patterns of Cu and CuGa NPs were acquired on a Thermo-Fisher Tecnai-Spirit at 120 kV. To analyze the samples after CO$_2$RR, the samples were prepared in the way same to described in the main text for STEM imaging.

Scanning electron microscopy (SEM) images were acquired with Thermo-Fisher Teneo using an in-lens (Trinity) detector at beam energy of 5 keV and current of 0.1 nA. Samples were imaged on the conductive glassy carbon substrates used as electrodes for CO$_2$RR measurements.

The content of Ga and Cu ions in the electrolyte after CO$_2$RR reaction was analyzed by Inductively Coupled Plasma Mass Spectrometry (ICP-MS) using kinetic energy discrimination (KED) mode with He as a collision gas on NexIon 350 D ICP-MS instrument (PerkinElmer). The samples were diluted 300 times with 2 % HNO$_3$ solution prior to the analysis. Y (yttrium) was added as an internal standard at concentration of 2 ppb to all the solutions. Absolute quantitation was performed using external calibration curve with standards in 0.05 – 50 ppb range. All measurements were performed in triplicates.

Electrochemically active surface area measurements

Electrochemically active surface area (ECSA) was determined via the Pb underpotential deposition (Pb UPD), which was performed in the same H-cell under N_2 atmosphere via cyclic voltammetry measurements in 0.1 M $KClO_4$ solution containing 0.002 M of $Pb(ClO_4)_2$ and 0.001 M KCl according to the previously reported protocol.[1,2] The solution was bubbled with N_2 prior to measurement, and no bubbling was allowed during the measurement; instead, N_2 was flowed over the electrolyte to avoid perturbation of the solution. The Pb UPD peak was integrated to obtain the catalyst electrochemically surface area, assuming that Pb coverage on CuGa surface is the same as for Cu (0.6 Pb atoms per Cu surface atom), which is reasonable as Cu and Ga are neighbors in the Periodic Table and have similar atomic radii. The reference value of 250 μC cm^{-2}_{Cu} was taken to quantify the NP surface.[1]

In Pb UPD tests, electrochemical impedance spectroscopy (EIS) was implemented prior to the main measurement to determine the electrochemical cell resistance (R_{cell}) and compensate for the ohmic losses. Four spectra were measured at the open-circuit potential, using 41 points between 1 MHz and 100 Hz, using a sinus amplitude of 20 mV and a pause time of 0.6 s between each frequency. A software utility in-built into the potentiostat software (EC-lab) was used to apply the ohmic loss correction to further measurement.

Linear combination analysis

Linear combination analysis of the Cu K- was carried out using the Prestopronto package.[3] For the Cu K-edge the references employed were a Cu foil and pressed samples of Cu_2O and CuO measured in transmission. Ordinarily, the use of transmission-based standards to model fluorescence yield data would be ill advised as a result of the latter suffering from the phenomenon of "self-absorption''. However, empirically it has been found that the electrode samples under study are so thin that the bulk references made in transmission are much more appropriate as standards to assess the speciation present than those same standards collected in fluorescence mode.

Using these three standards, different models were applied, for instance, Cu foil, Cu foil + CuO, Cu foil + Cu_2O, and Cu foil + Cu_2O +CuO, to fit the data and a comparison made of the how the statistical measured of goodness of fit (Chi^2) changed between each model and with time. From this comparison it was then determined whether or not the addition or replacement of a given reference had a significant effect (positive or negative) on the ability of the model to fit the XANES data.

Surface oxide thickness calculation from linear combination analysis

The thickness of the surface oxide on the NPs surface was calculated assuming spherical shape of the NPs. With this, and with the assumption that the mass and atomic fractions of the oxide are similar (x, %), the surface oxide thickness, r_{ox} (nm), is calculated as:

$$V_{total} = \frac{4\pi r_{total}^3}{3}$$

$$V_{core} = \frac{4\pi r_{core}^3}{3} = (1 - x)V_{total} = (1 - x)\frac{4\pi r_{total}^3}{3}$$

$$r_{core} = \sqrt[3]{(1 - x)}\, r_{total}$$

$$r_{ox} = r_{total} - r_{core} = \left(1 - \sqrt[3]{(1 - x)}\right) r_{total}$$

EXAFS data processing and analysis

Analysis of the extracted EXAFS data was performed using EXCURV (v. 9.3).[4] In terms of reporting the analysis, we have confined ourselves by and large to only analyses of the first coordination M – M shell (N1), its associated bond distance (d, Å) and disorder parameter (the Debye-Waller factor (DWF), Å^2).

E_F refers to the edge position relative to Vacuum zero (Fermi energy, eV), and the AFAC parameter (0.9 in all cases), determined through fitting of a copper foil standard relates to the proportion of electrons undergoing scattering post absorption that contribute to the EXAFS. In assessing the quality of the fits obtained, the R-factor (R%) is defined as follows as follows:

$$R = \sum_i^N \frac{1}{\sigma_i}(\chi_i^e(k) - \chi_i^t(k))^2 \cdot 100\%$$

where $\chi_i^e(k)$ and $\chi_i^t(k)$ are the experimental and theoretical EXAFS, respectively, and k is the photo-electron wave-vector (Å^{-1}). σ_i is the uncertainty in the data, with

$$\frac{1}{\sigma_i} = \frac{k_i^n}{\sum_j^N k_i^n \left(\chi_i^e(k_j)\right)^2}$$

The fitting range used in R space (δR) was 1 – 3, whilst the range of k space used for the fitting of the EXAFS was between 2.5 – 3 and 12.5 – 13 (Å^{-1}) (**Figures S21 – S23**).

Density functional theory calculations

Density Functional Theory (DFT) calculations, adopting the Pardew Burke Ernzerhof (PBE) functionals, were performed through the CP2K suite.[5] The DZVP-MOLOPT basis set was adopted in the calculations, where core electrons are represented as per the dual-space

Goedecker–Teter–Hutter pseudopotential framework.[6,7] The planewave cut-off was set to 500 Ry (relative cut-off of 50 Ry). The DFT self-consistent loops to estimate the system total energy were considered as converged when a difference lesser than 10^{-8} Ry was found between two successive iterations. A Fermi-Dirac smearing with an electronic temperature of 300K was adopted in the calculations.

An *fcc* structure was considered for Cu and Cu-rich phases, in agreement with experimental measurements. For the Cu-rich phases, 3 and 12 Cu atoms are respectively substituted in the Cu slab with Ga atoms. Lattice distances are then modified according to Vegard's law. The (111) facet was chosen to inspect properties of the Cu-rich system, as the latter is the most energetically favorable one in Cu. A (4×4) slab with 4 layers, with periodicity along the slab plane was considered. The Cu_9Ga_4 phase was used to model the properties of the CuGa37 sample. 4 layer slabs were also considered for this system. For reference, snapshots of the DFT configurations are displayed in **Figure S4**. Input and outputs are also available from the Materials Cloud (https://doi.org/10.24435/materialscloud:ft-s8).

To assess changes in the electronic structure of the system as a function of the Ga content, we evaluated the Bader charge density of the candidate adsorption site in relaxed slabs, or neighboring Ga atom, utilizing the algorithm and code developed by Henkelman and coworkers.[8] The slab lowermost and next lowermost layers were kept fixed during each structural relaxation. These calculations were considered converged when all the atomic forces resulted less than 0.5 meV $Å^{-1}$.

We calculated the formation energy of COH from adsorbed CO, ΔE_{COH}, within the computational hydrogen electrode model:

$$\Delta E_{COH} = E_{*COH} - E_{*CO} - E_{H2}/2$$

Where E_{COH} and E_{CO} is the energy found for adsorbed CO and CHO on the catalyst, and E_{H2} is the energy of an H_2 molecule in the gas phase. To evaluate COH formation energy on *fcc*(111) slabs we considered CO adsorbed at top site (to match experimental observations) and COH adsorbed at a hollow site. To evaluate COH formation on the Cu_9Ga_4 slab, we first probed CO adsorption energies on Cu non-equivalent adsorption sites, and report ΔE_{*COH} for the site where CO adsorption is the most favorable. Screening of sites in another Cu_9Ga_4 energetically competitive surface,. i.e. (110), results in an even larger ΔE_{*COH}.

To probe, in a qualitative (if not quantitative) fashion, the tendency of Cu, CuGa4, CuGa17, and Cu_9Ga_4 systems to undergo structural rearrangements, we assessed their finite temperature stability by means of *ab initio* Molecular Dynamics. Newton's equation of motions are

integrated with a 2 fs time step while a Canonical Sampling through Velocity Rescaling (CSVR) thermostat with time constant of 30 fs is used to regulate the temperature of the system. The slab lowermost layer was kept fixed during dynamics. Inputs were gathered and stored in the Materials Cloud repository.

To contain the computational cost of the simulation while retaining robust statistics, we sampled the system evolution over 10 independent trajectories of 0.75 ps at 407 K and 678 K, respectively one third and one half of the Cu melting temperature. We observed no structural rearrangements for Cu-rich slabs. These systems appear stable also when extending the sampling up to 1 ps. Viceversa, we witnessed significant restructuring in the Cu_9Ga_4 structure, at both 407 K (1 simulation), and 678 K (3 simulations), notwithstanding the short simulation timescale. An example of the observed structural rearrangement is highlighted in **Figure S30**. These results are well-aligned with the thermal stability of the bulk phases, with Cu-rich phases being largely more robust to melting than the Cu_9Ga_4 phase.
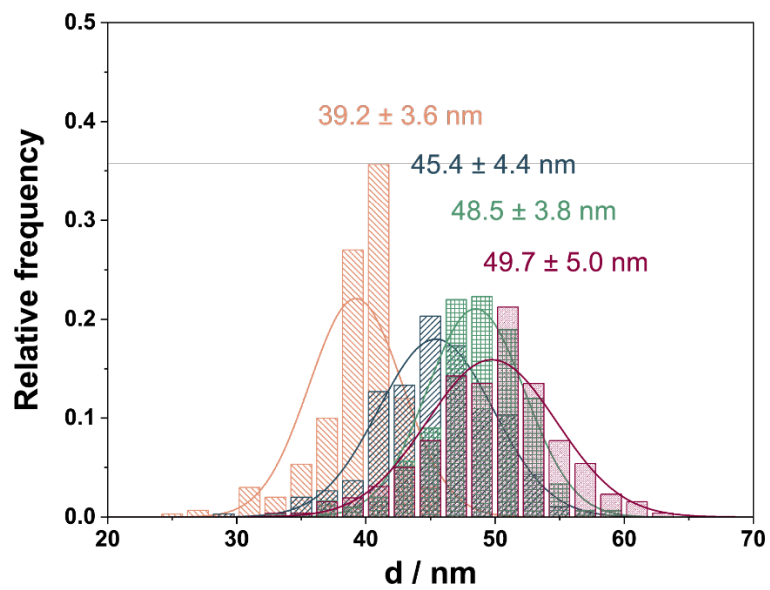
Figure S1. Size distributions of Cu, CuGa4, CuGa17 and CuGa37. The size grows according to the fact that Ga, which has larger radius than Cu, is incorporated in the lattice.
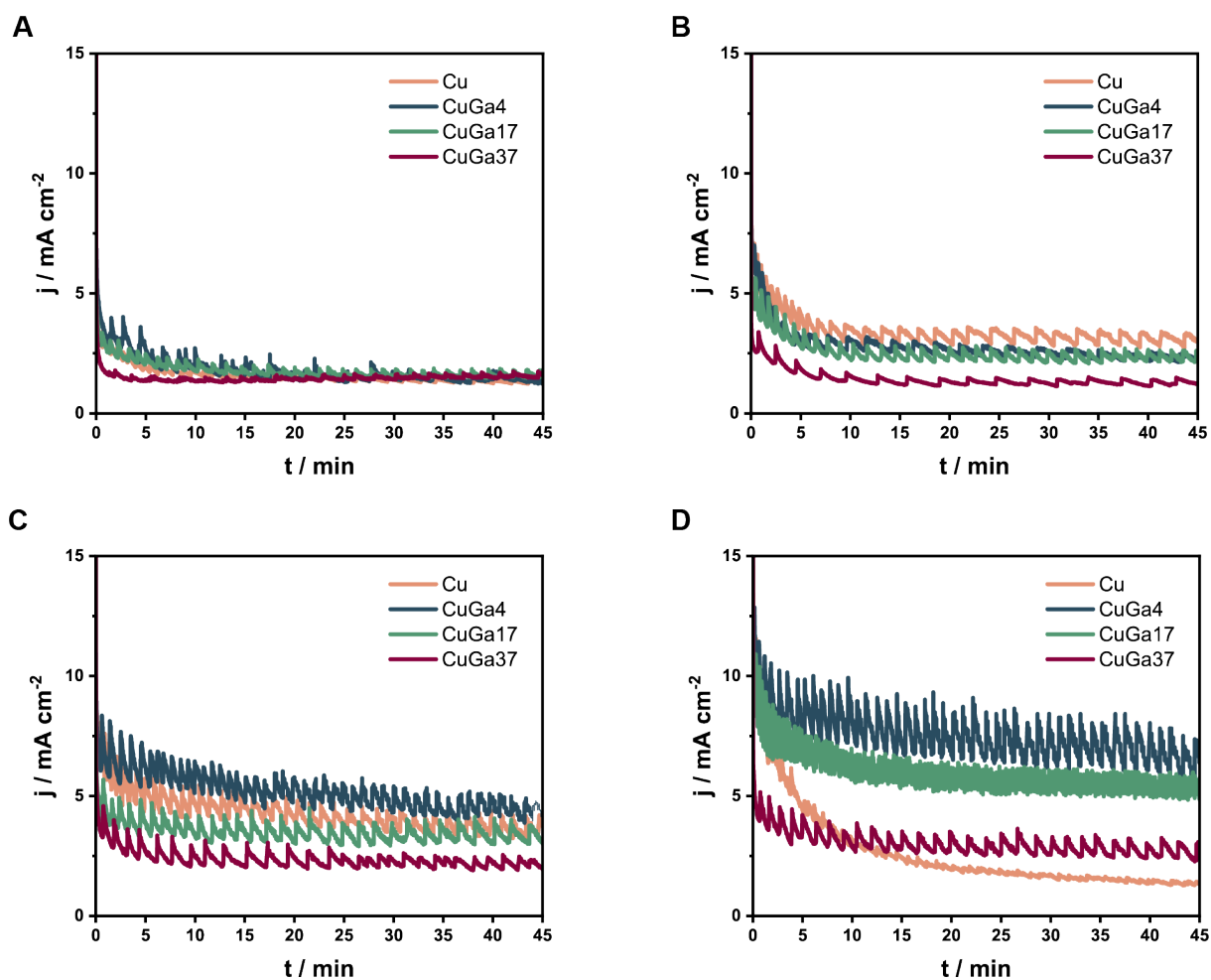
**Figure S2.** Current densities of (A) Cu, (B) CuGa4, (C) CuGa17 and (D) CuGa37 NPs during 45 min of CO_2RR at -1.2 V_{RHE} in CO_2-saturated 0.1 M $KHCO_3$. The spikes on the chronoamperometry profiles are attributed to the bubbles formation on the electrode surface.
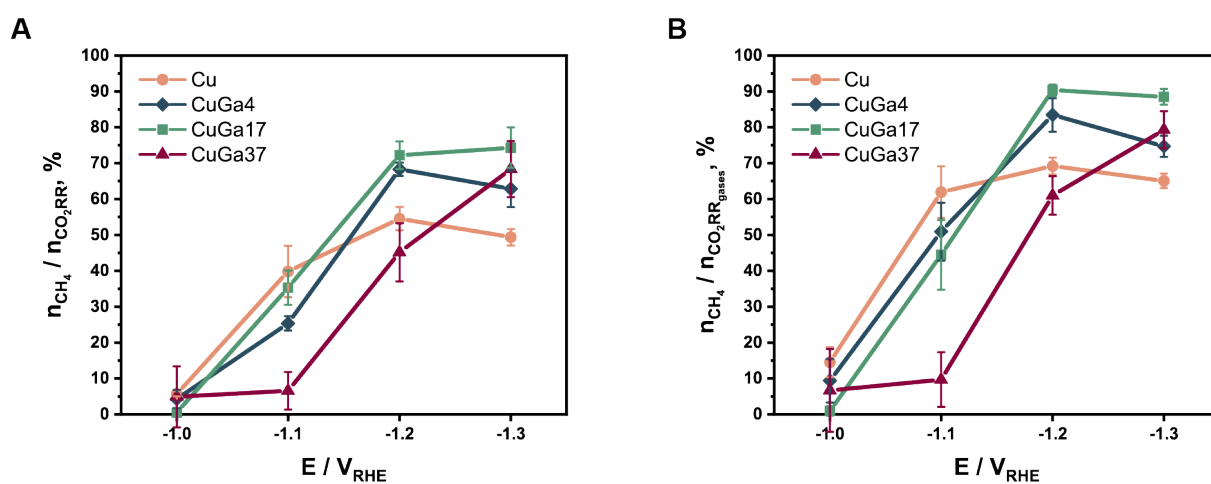
Figure S3. Molar fraction of CH_4 among (A) all CO_2RR products and (B) gaseous CO_2RR products for Cu, CuGa4, CuGa17 and CuGa37 NPs during 45 min CO_2RR in CO_2-saturated 0.1 M $KHCO_3$ at different voltages.
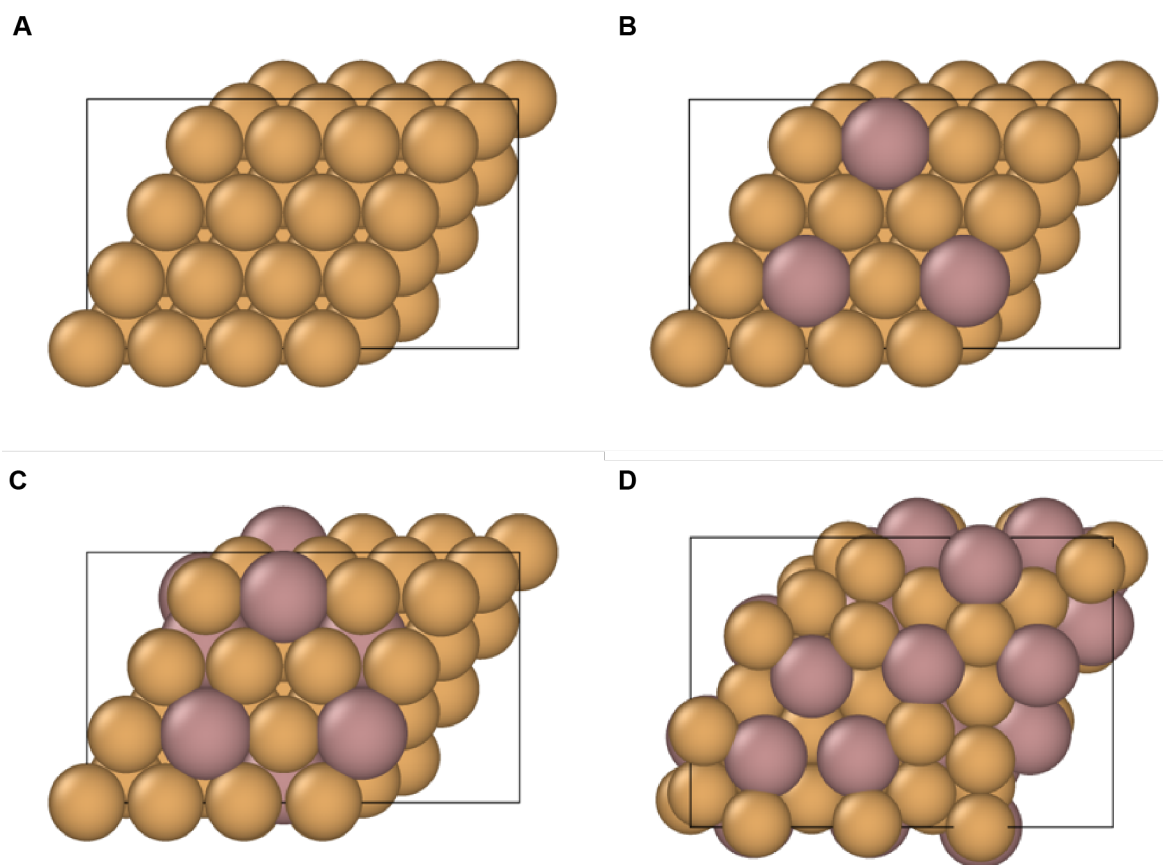
Figure S4. Slabs used for the DFT calculations, with pale red Ga atoms and brown Cu atoms; (111) surfaces are selected for the *fcc* structures (A) Cu, (B) CuGa4 (Cu96Ga4 slab), (C) CuGa17 (Cu82Ga18) and (D) (033), with distorted densely packed Cu layers, for CuGa37 (Cu$_9$Ga$_4$-type cell). For Cu96Ga4 slab, arrangement with Ga atoms on the surface rather than in subsurface layer is selected, as it is more representative of the elemental distribution within CuGa4 nanoparticles.
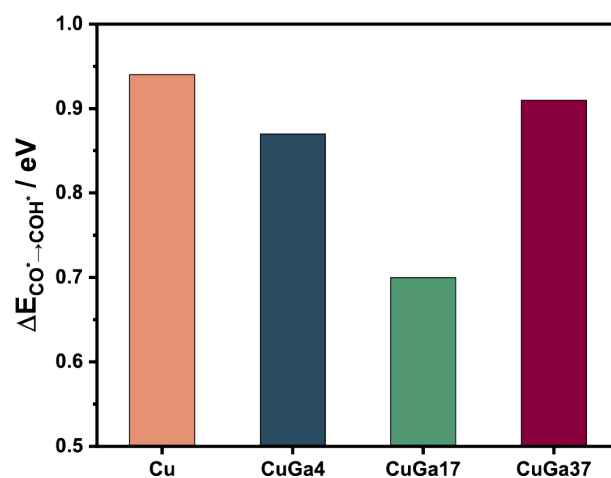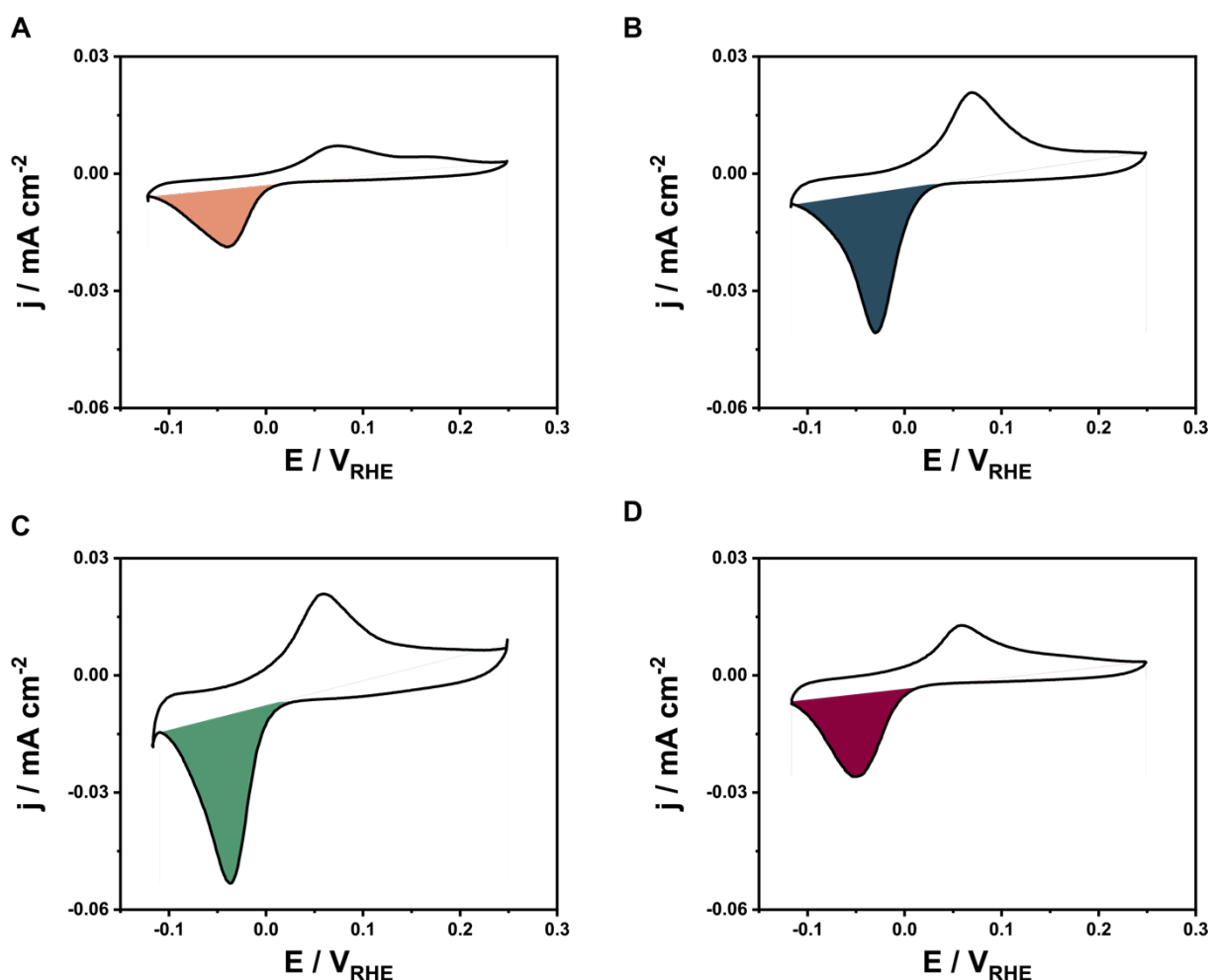

Figure S5. DFT calculations of the CO protonation energy for Cu and CuGa alloys.

Table S1. Electrochemically active surface (ECSA) areas for Cu, CuGa4, CuGa17 and CuGa37 determined by Pb underpotential deposition (UPD) performed after 45 min CO_2RR at -1.0 V_{RHE}.

Cu	CuGa4	CuGa17	CuGa37
0.51 ± 0.06 cm^2	1.11 ± 0.02 cm^2	1.29 ± 0.02 cm^2	0.66 ± 0.09 cm^2

Figure S6. Characteristic cyclic voltammetries of (A) Cu, (B) CuGa4, (C) CuGa17 and (D) CuGa37 NPs in N_2-saturated 0.1 M $KClO_4$ solution containing 0.002 M of $Pb(ClO_4)_2$ and 0.001 M KCl after 45 min CO_2RR at -1.0 V_{RHE}.

The two main methodologies employed to determine the electrochemically active surface area (ECSA) for Cu-based electrocatalysts are capacitance measuraments and metal UPD. The former requires a potential range where no faradaic process occurs. We could not find a suitable potential range, where no faradaic process occur, in order to properly perform capacitance measuraments. Thus, we turned into Pb UPD.

Pb UPD is a technique with great potential when it comes to surface characterization of bimetallic electrocatalysts.[2,9] The surface composition can be in principle determined. However, reference samples of both metals alone are needed. In the case of Cu and Ga, Ga is liquid at room temperature, so its structure has nothing to do with that of the Cu-Ga alloyed NPs and cannot be regarded as a valid reference. In the absence of appropriate reference samples, we do not correlate the UPD to the alloy composition and we cannot conclude about its element specificity.

Furthermore, we note that Cu NPs reconstruct quite substantially during CO_2RR, which implies changes in their ECSA. For this reason, we decided to measure the Pb UPD after 45 minutes CO_2RR at -1.0 V_{RHE} as a good approximation of their ECSA under operation.

The data show that CuGa4 and CuGa17 have similar ECSA, which is higher than the pristine Cu and of CuGa37 and suggests a higher number of active sites. CuGa37 possesses a different crystal structure to Cu, thus a direct comparison with other samples is challenging.

Based on the fact that all these uncertainties exist, we report only the geometric current densities in the main text and do not discuss changes in the intrinsic activity of Cu when alloyed with Ga. However, we report the partial current densities normalized by ECSA below as **Figure S7**.

The ECSA-normalized j_{CO2RR} suggests that intrinsic activity of the catalysts towards CO_2RR decreases from Cu to CuGa4, CuGa17 and CuGa37 below -1.2 V_{RHE}, while the alloy NPs surpass Cu at -1.3 V_{RHE} (**Figure S7A**). The increase in intrinsic activity at -1.3 V_{RHE} is attributed to CH_4 promotion (**Figure S7B**) as changes in the intrinsic activity for C_2H_4 are more subtle (**Figure S7C**). The ECSA-normalized j_{H2} increases from CuGa4 and CuGa17 NPs to CuGa37 (**Figure S7D**), which has larger amount of Ga and probably Ga-rich domains on the surface. Ga by itself produces mostly H_2 at this operation conditions,[10,11] which explains this increase in j_{H2} for this sample.
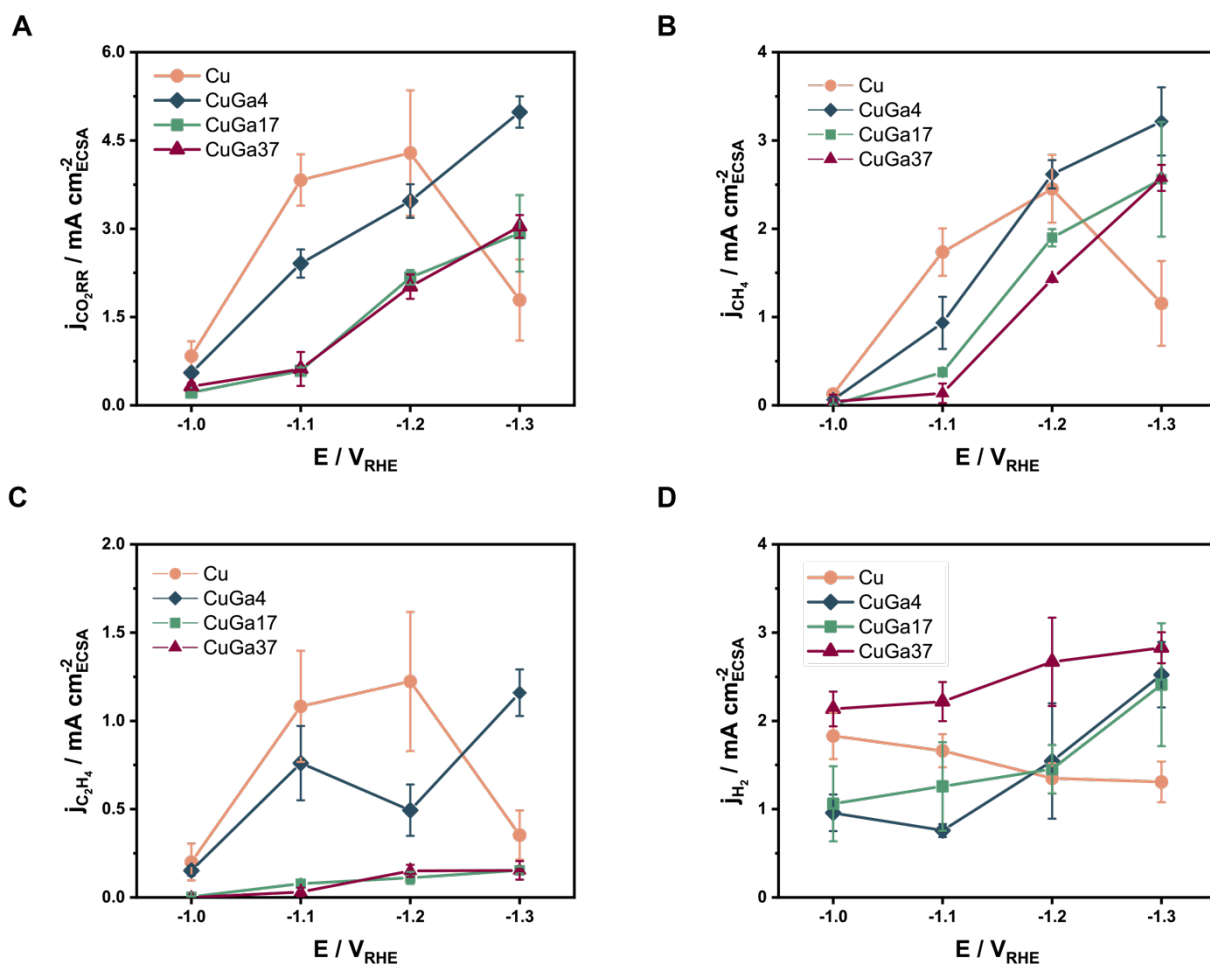
Figure S7. ECSA-normalized partial current densities towards (A) all CO_2RR products, (B) CH_4, (C) C_2H_4 and (D) H_2 for Cu, CuGa4, CuGa17 and CuGa37 NPs averaged over 45 min of CO_2RR in CO_2-saturated 0.1 M $KHCO_3$ at different operation voltages.
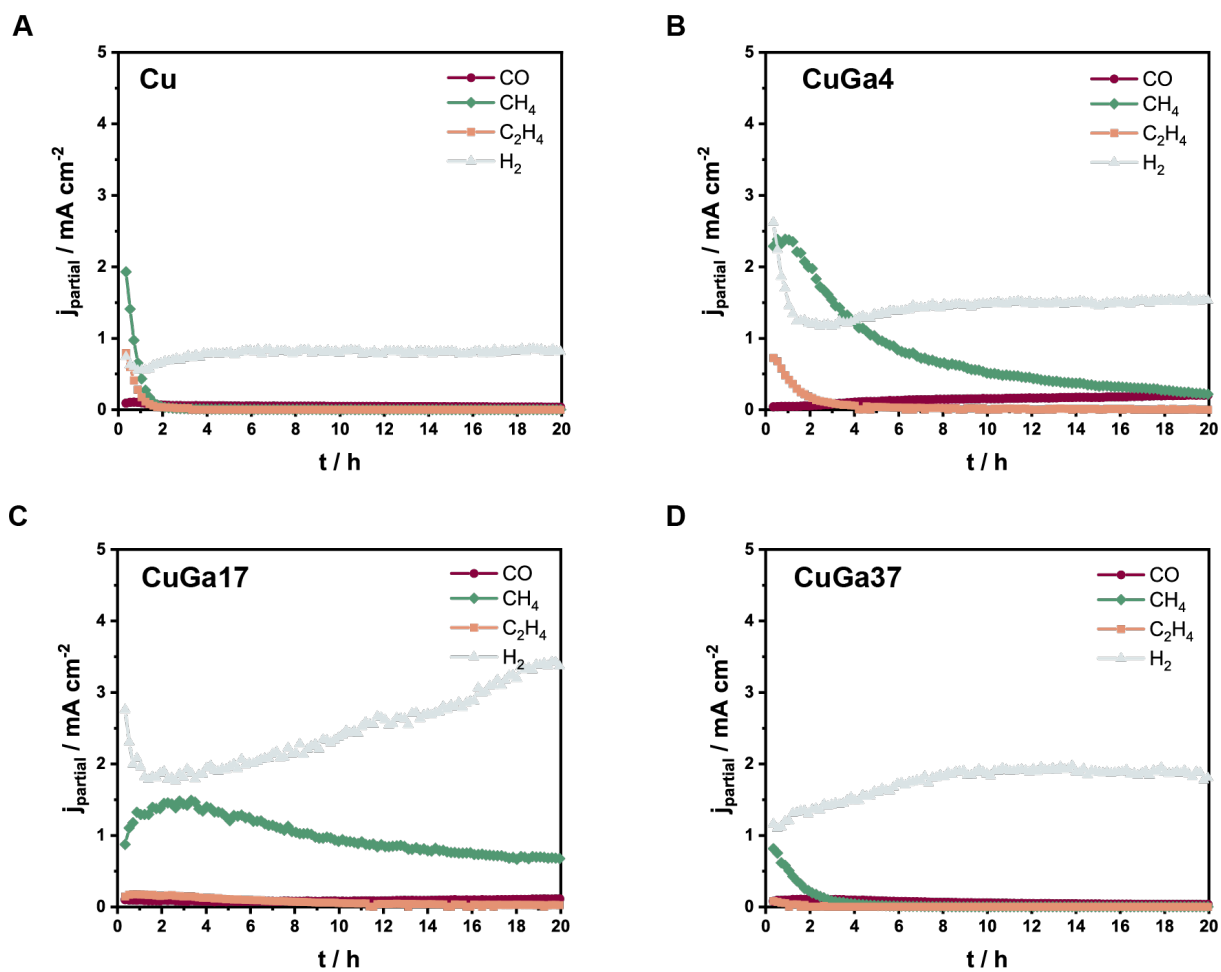
Figure S8. Evolution of the partial current densities towards gas products for (A) Cu, (B) CuGa4, (C) CuGa17 and (D) CuGa37 NPs during 20 h of CO_2RR at -1.2 V_{RHE} in CO_2-saturated 0.1 M $KHCO_3$.
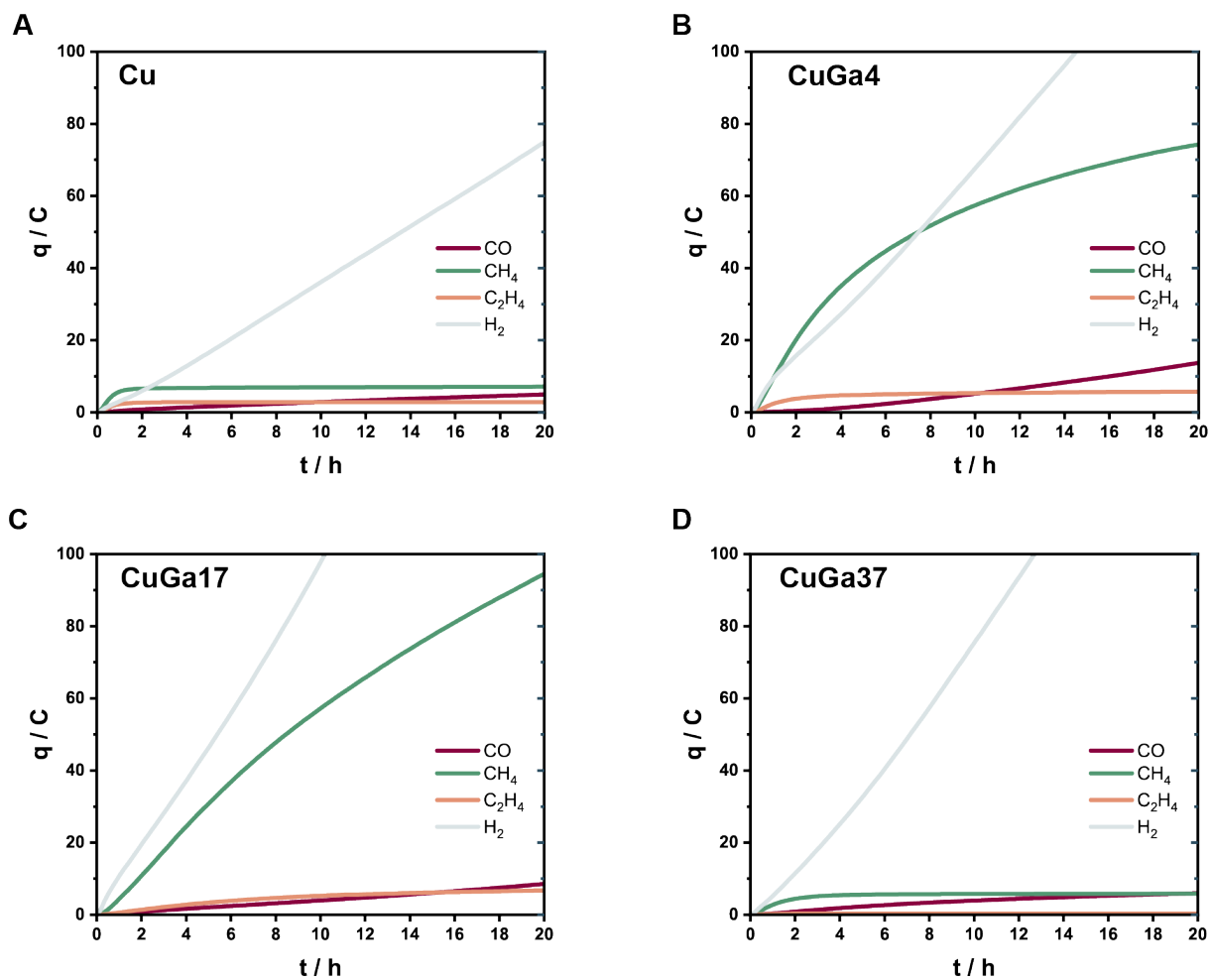
Figure S9. Accumulated charge consumed towards the formation of different gaseous products (CO, CH_4, C_2H_4 and H_2) for (A) Cu, (B) CuGa4, (C) CuGa17 and (D) CuGa37 NPs during 20 h of CO_2RR at -1.2 V_{RHE} in CO_2-saturated 0.1 M $KHCO_3$.
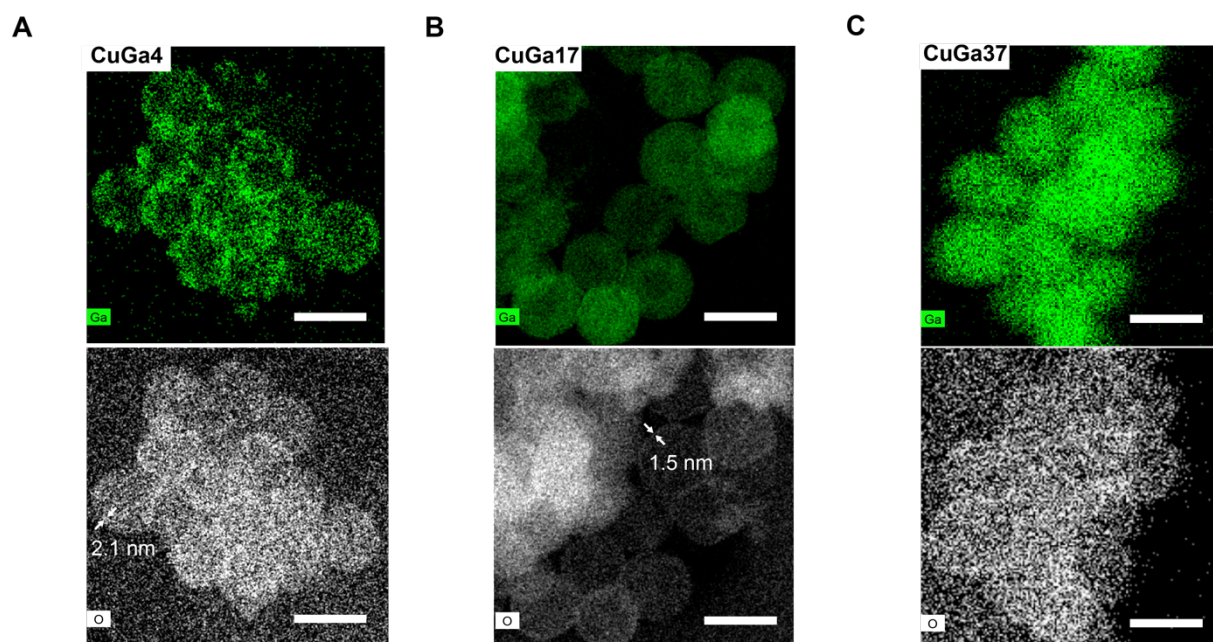
**Figure S10**. STEM-EDXS elemental mapping (Ga – green, O – white) for (A) CuGa4, (B) CuGa17 and (C) CuGa37 NPs in as-synthesized state. The scale bar is 50 nm. Increased O signal in the regions without NPs is attributed to the O on the TEM grid. The oxidized shell is less evident in CuGa37, as there is no surface Ga enrichment evident on the map, and both Cu and Ga are exposed (**Figure 5**).
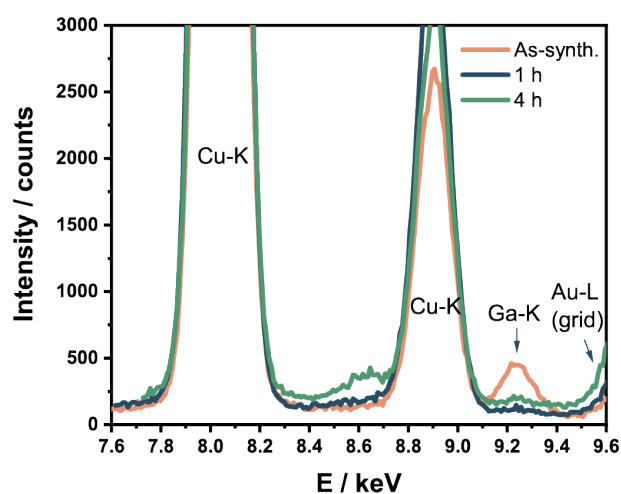

Figure S11. STEM-EDXS spectrum of CuGa4 sample after (A) for as-synthesized NPs and after (B) 1 h and (C) 4 h CO_2RR at -1.2 V_{RHE} in CO_2-saturated 0.1 M $KHCO_3$.
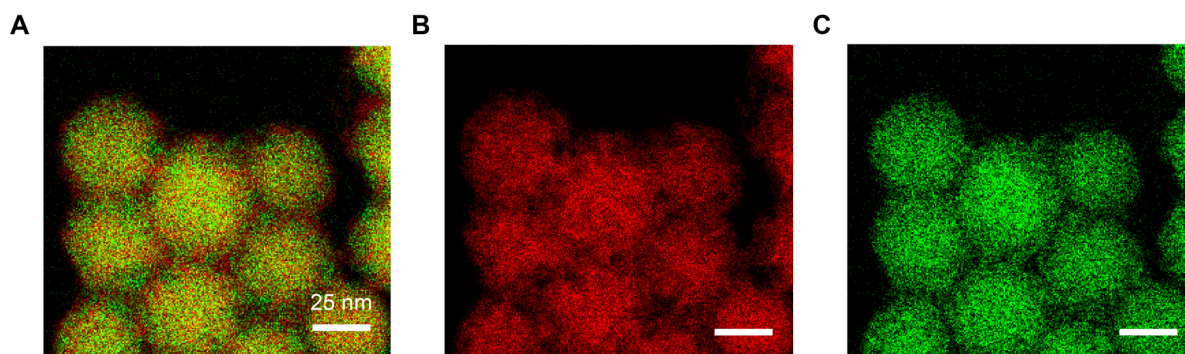
Figure S12. (A) STEM-EDXS elemental mapping (Cu – red, Ga – green) and single-element STEM-EDXS maps for (B) Cu and (C) Ga for CuGa37 NPs after 4 h CO_2RR at -1.2 V_{RHE} in CO_2-saturated 0.1 M $KHCO_3$. The region of interest corresponds to the map reported in **Figures 4, 5**, but is presented at higher magnification to highlight the changes on the NPs surface.
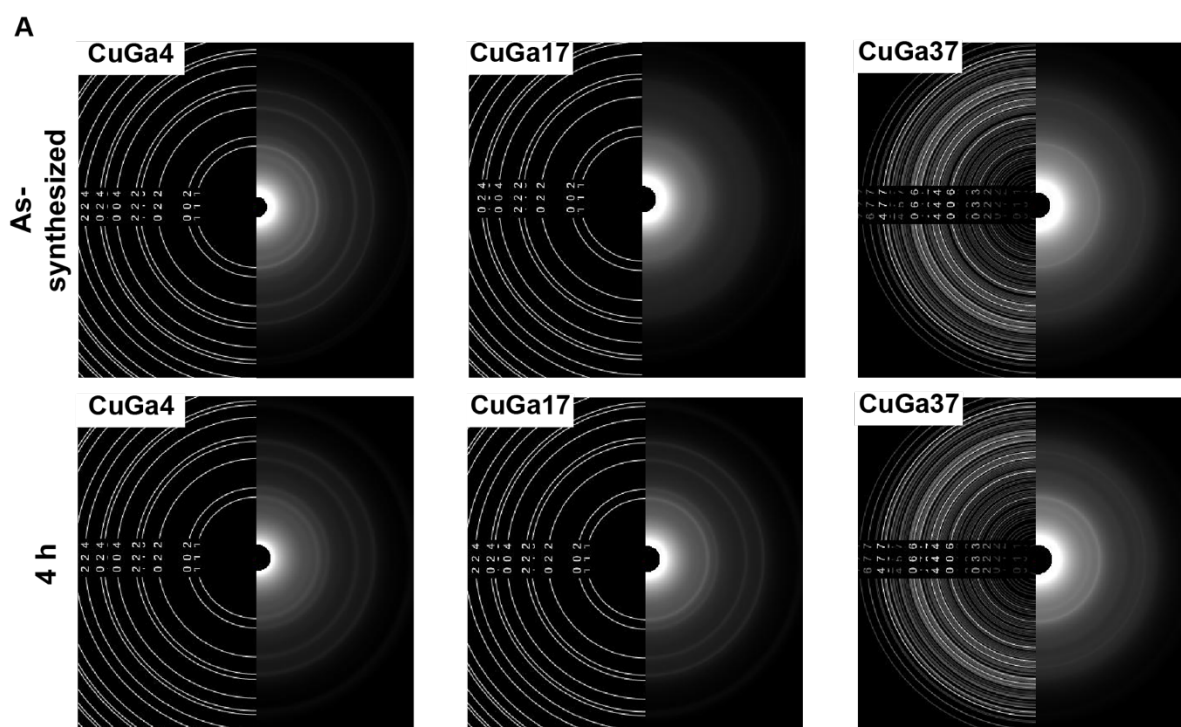
Figure S13. SAED patterns of Cu, CuGa4, CuGa17 and CuGa37 NPs in as-synthesized state and after 4 h electrolysis at -1.2 V_{RHE} in CO_2-saturated 0.1 M $KHCO_3$.
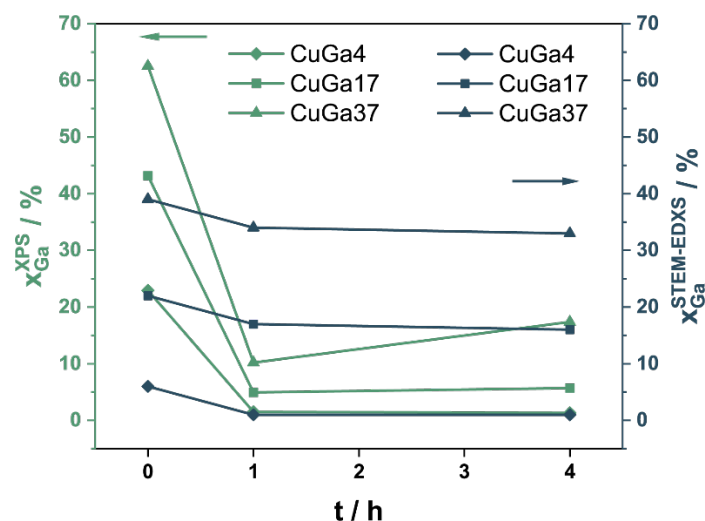
Figure S14. XPS and STEM-EDXS quantification of Ga content in CuGa4, CuGa17 and CuGa37 NPs in as-synthesized state and after 1 h and 4 h of CO_2RR at -1.2 V_{RHE} in CO_2-saturated 0.1 M $KHCO_3$. Surface Ga enrichment in the pristine samples correlates with the presence of Ga-rich shell which is removed after the CO_2RR.
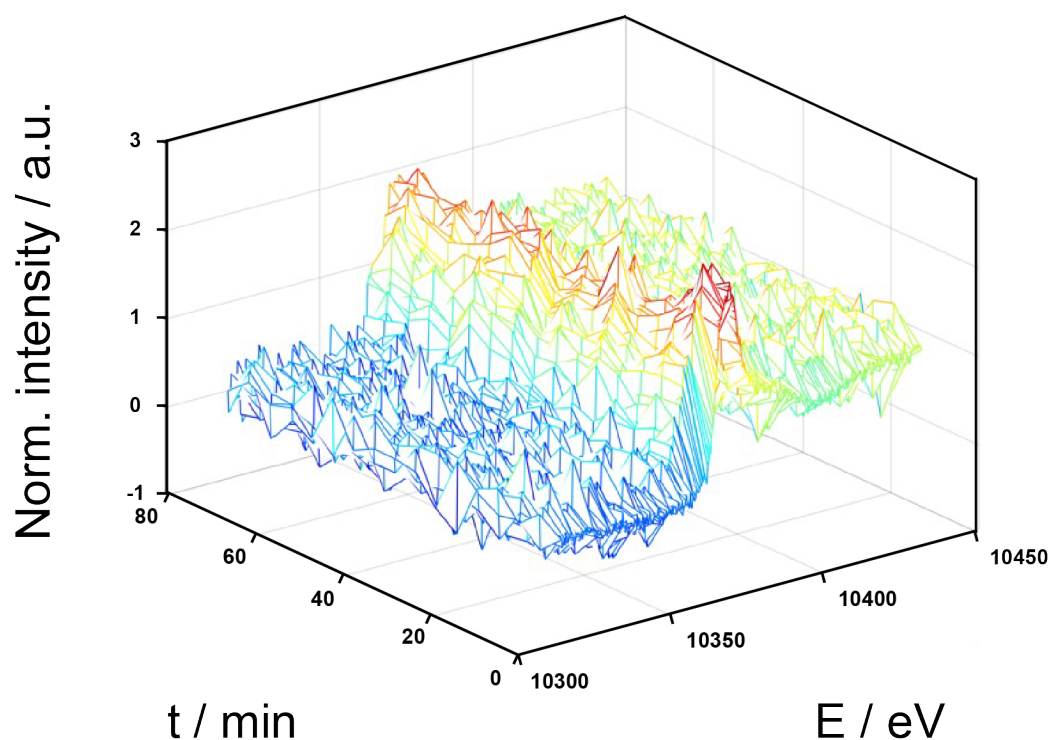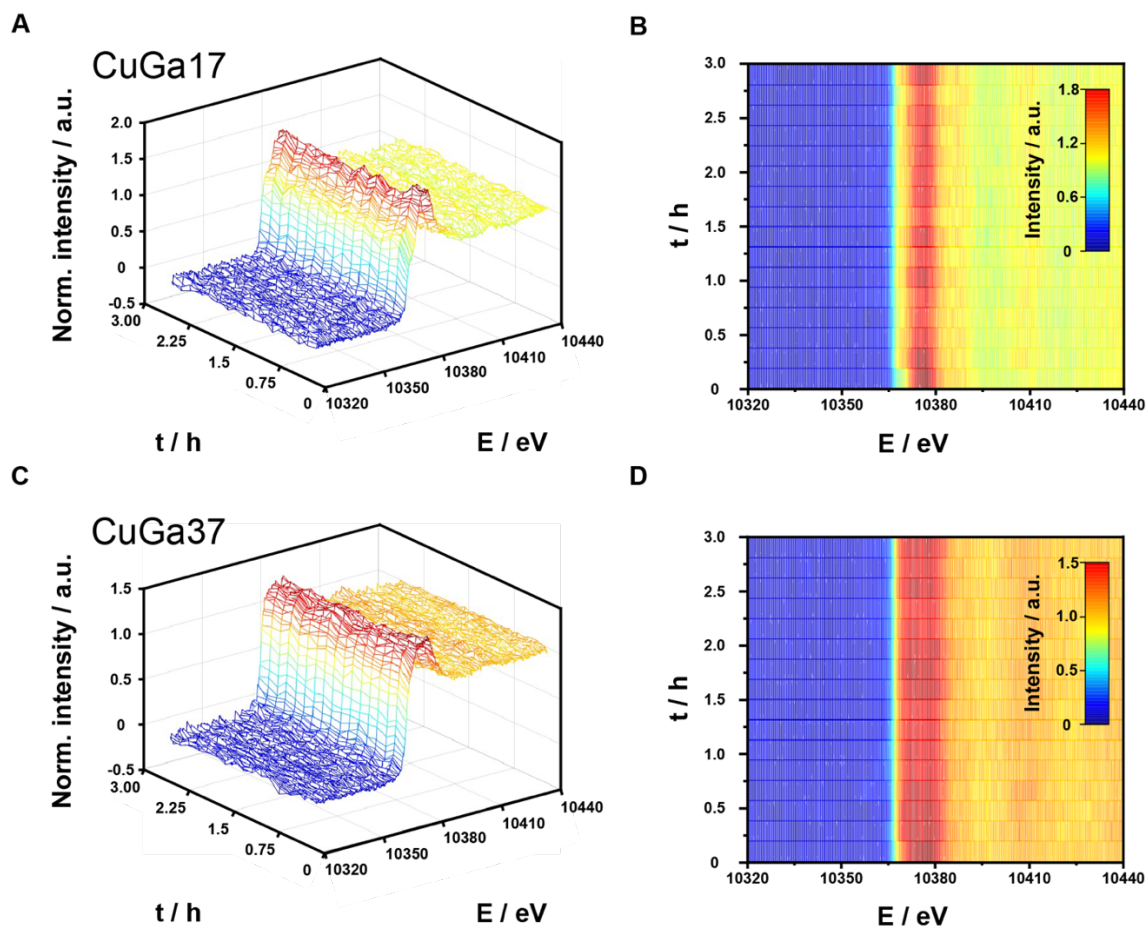

Figure S15. Ga K-edge *operando* XANES 3D map of CuGa4 during CO_2RR at -1.2 V_{RHE} in CO_2-saturated 0.1 M $KHCO_3$, confirming that Ga is present in the sample over the course of electrolysis.
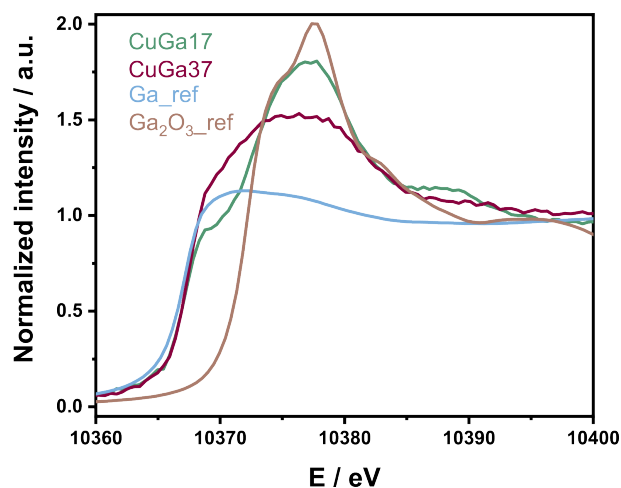
Figure S16. Ga K-edge XANES spectra at ocp in CO_2-saturated 0.1 M $KHCO_3$ for CuGa17 and CuGa37 NPs. The standards were bulk materials and measured *ex situ*.

Figure S17. (A – D) Ga K-edge *operando* XANES spectra during 3 h CO_2RR at -1.2 V_{RHE} in CO_2-saturated 0.1 M $KHCO_3$ for (A, B) CuGa17 and (C, D) CuGa37 NPs: (A, C) 3D maps in time – energy – normalized intensity coordinates and (B, D) corresponding 2D maps in time – energy coordinates. Averaging was performed over every five consecutive scans.
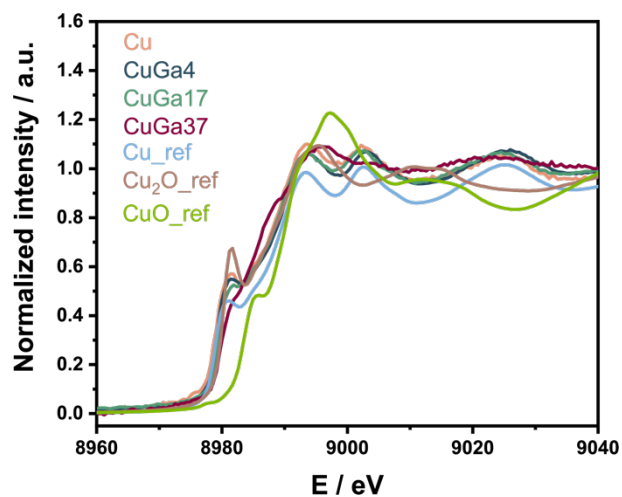
Figure S18. Cu K-edge XANES profile for Cu and CuGa alloy NPs during CO$_2$RR at ocp in CO$_2$-saturated 0.1 M KHCO$_3$ together with bulk Cu standards (standards were measured *ex situ*, being foil for Cu and pelletized powders for Cu$_2$O and CuO).
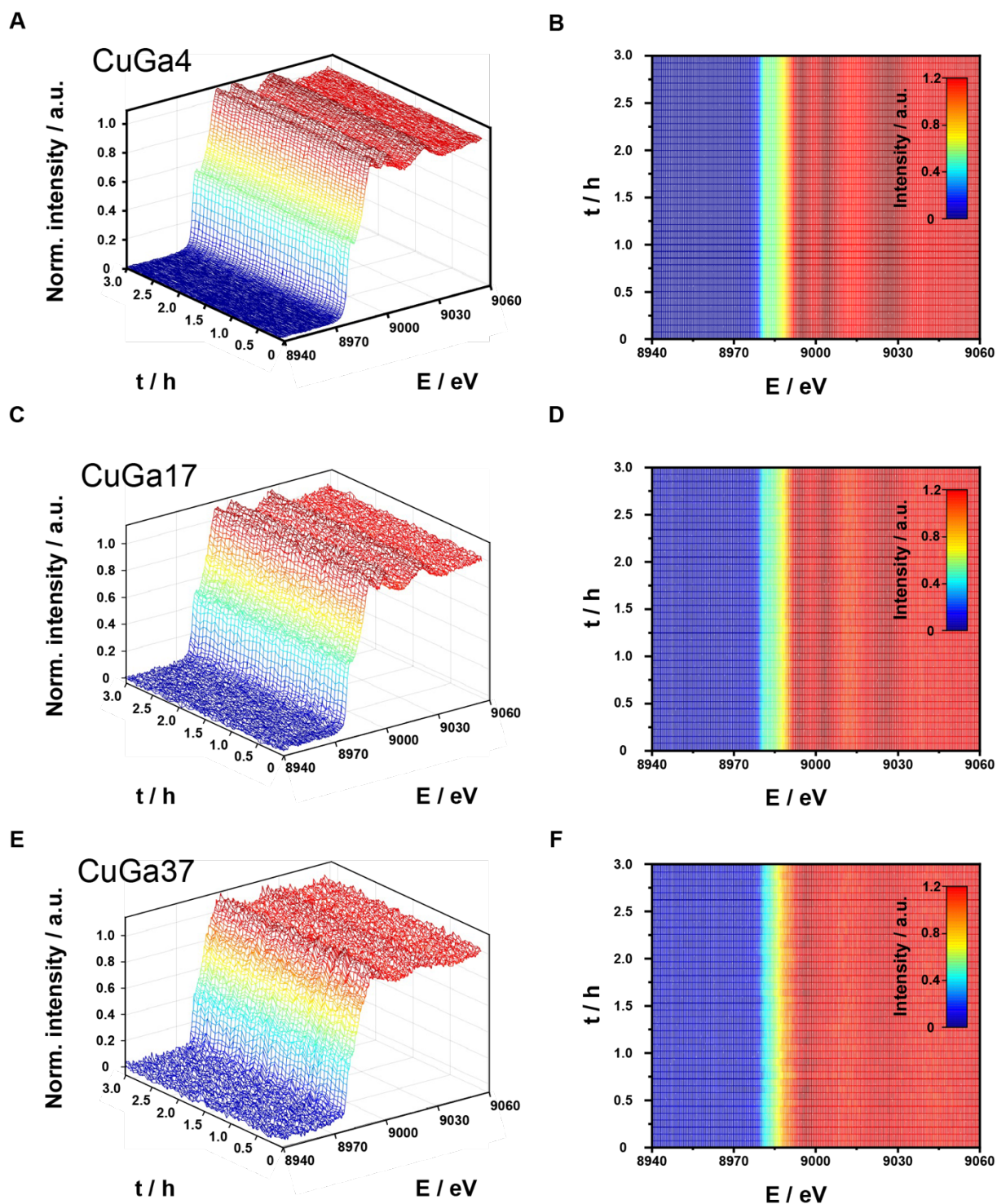
Figure S19. Cu K-edge *operando* XANES spectra during 3 h CO_2RR at -1.2 V_{RHE} in CO_2-saturated 0.1 M $KHCO_3$ for (A, B) CuGa4, (C, D) CuGa17 and (E, F) CuGa37 NPs: (A, C, E) 3D maps in time – energy – normalized intensity coordinates and (B, D, F) corresponding 2D maps in time – energy coordinates. Averaging was performed over every two consecutive scans.
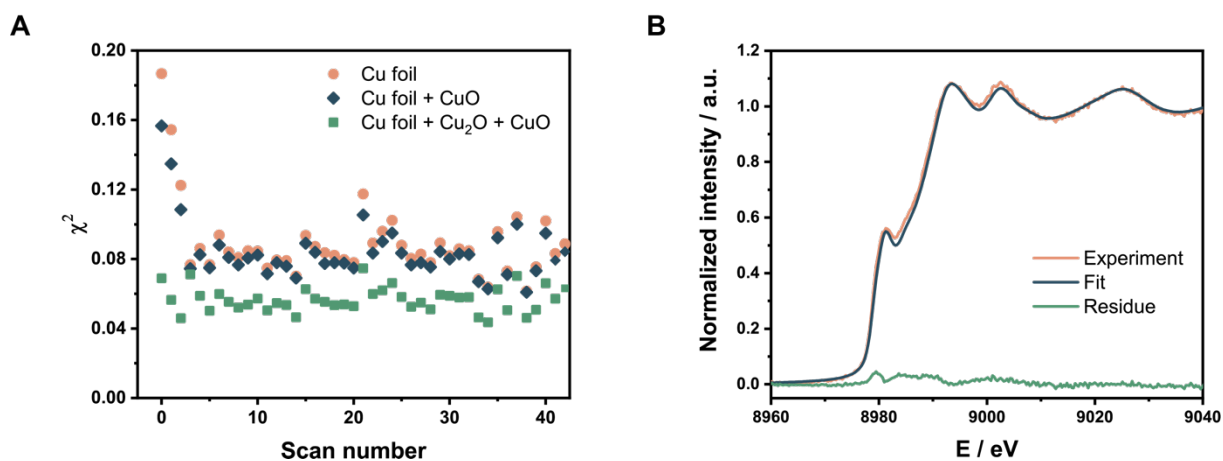
LCA details.

Figure S20A shows the variation of Chi^2 squared observed using different LCA modes to describe the Cu XANES data collected during CO_2RR over the CuGa4 system. **Figures S20B** shows the characteristic fit to the data and corresponding residual derived from the start of the experiment.

Figure S20. (A) Variation of goodness of fit (Chi^2) obtained for different LCA models (as indicated) of the Cu K-edge XANES derived from the CuGa4 system during CO_2RR. (B) Comparison of the experimental Cu K-edge XANES, the best derived fit and residuals for the start of the CO_2RR measurement.

As it can be seen in **Figure S20B**, the use of the bulk standards collected in transmission mode yields a good fit to the operando XANES. Most significantly, from **Figure S20A**, the effects of the quality of the fitting as different components are added can be clearly derived as a function of time (scan number) during the CO_2RR experiment. Furthermore, the most significant variations in Chi^2 as a function of the model applied can be observed at the start of the experiment, and that of the oxidic standards it is Cu_2O, rather than CuO that has the most significant effect on the goodness of fit obtained when included with the metallic copper component (Cu foil). At a lower level, and throughout the CO_2RR this benefit to the goodness of fit is then maintained throughout the experiment. From this it is concluded that the starting materials is predominantly comprised of a metallic copper phase upon which a layer of Cu_2O like materials exists which is largely removed during the first mins of CO_2RR operation.

EXAFS interpretation details. **Figures S21, S22** show the K^3-weighted EXAFS obtained for Cu, CuGa4, CuGa17 and CuGa37 NPs both before and under operation conditions (at -

1.2 V_{RHE}). **Figure S23** gives the equivalent Ga K-edge EXAFS for the CuGa17 and CuGa37 cases. **Figures 7F,G** report the EXAFS spectra as Fourier-transfromed intensities *vs.* interatomic distances for Cu and Ga. In these cases, only the first shell Cu-M interaction has been fitted even though it is clear from the Fourier Transforms in all cases save for the CuGa37, that significant *fcc* higher shell structure, which is subject to variation, is present.

Ordinarily, when reporting EXAFS analysis, only single values, along with estimates of likely errors, for coordination numbers, bond distances and Debye-Waller factors are given. However, whilst such a reportage may be sufficient in the current cases, it is deemed more informative, and indeed realistic, to explicitly present aspects of the correlations that exist between certain parameters, such that the likely range of values for, for instance, the highly correlated first-shell coordination number (N1) and disorder parameter (Debye-Waller factor, $Å^2$), and apparent changes in the first-shell bond distances (d, Å), as and where they occur, might be better gauged and their likely sources more precesely defined.

As such, **Figures S24 – S29** give correlation plots that relate various of these parameters, as indicated, to the quality of the fitting as given by the R-factor (R%, as given by the coloured bar to the right of each of the correlation plots) and provide a comprehensive picture of the structural changes occurring between ocp and -1.2 V_{RHE}. **Table 1** summarises the results obtained from analysis of the EXAFS data (in k space) in each case.
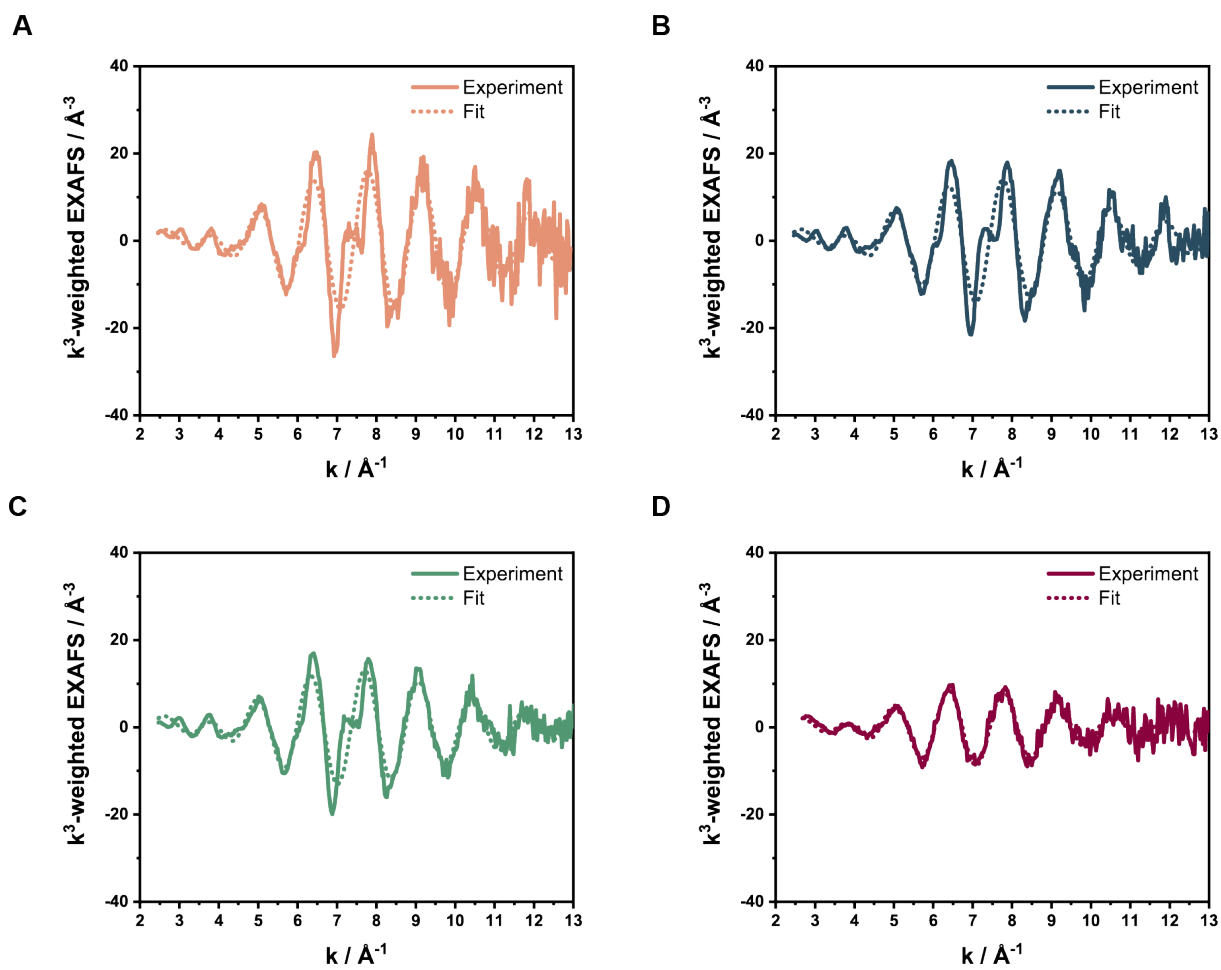
Figure S21. Experimental and fitted Cu K-edge EXAFS profiles in k-space at ocp for (A) Cu, (B) CuGa4, (C) CuGa17 and (D) CuGa37 NPs.
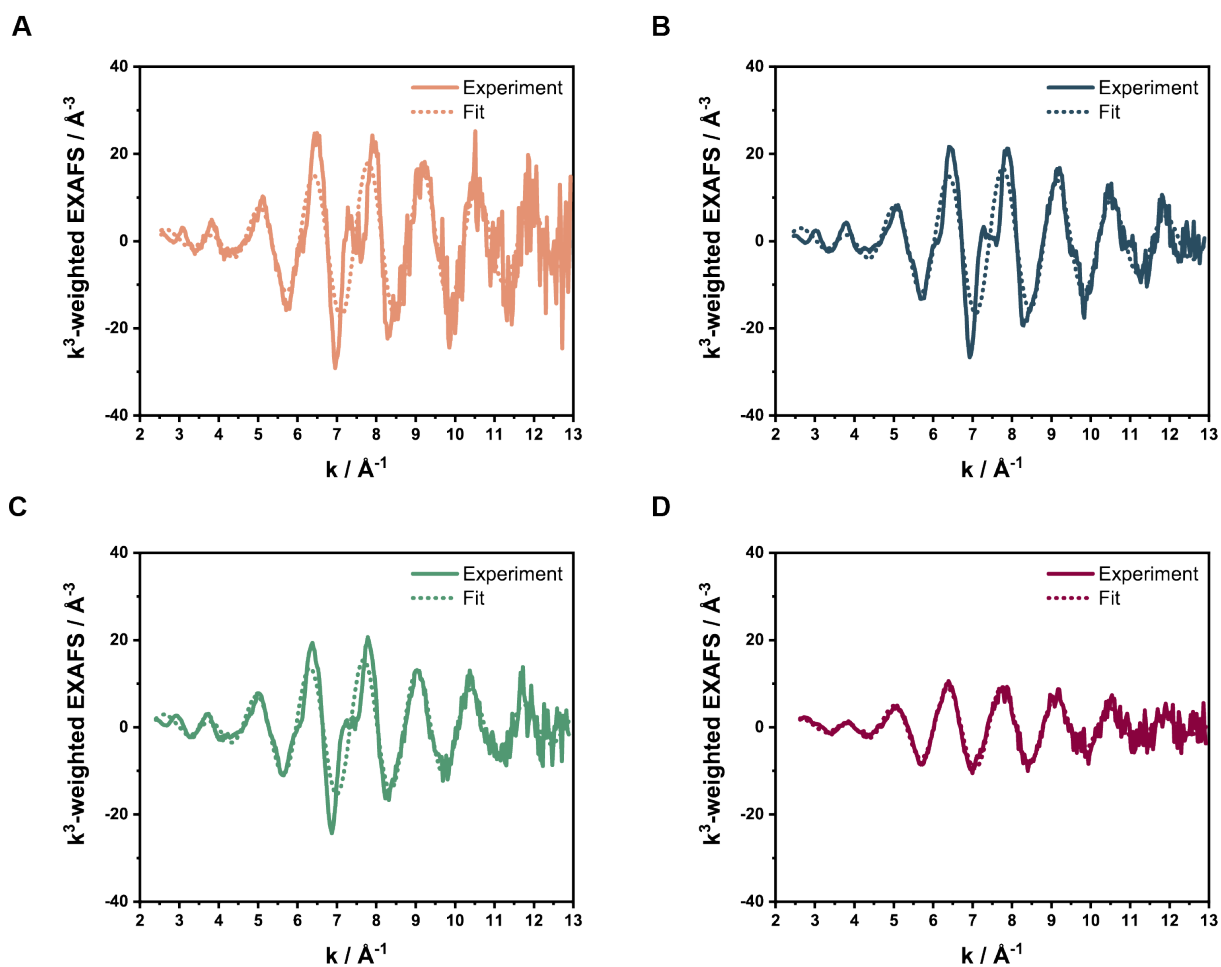
Figure S22. Experimental and fitted Cu K-edge EXAFS profiles in k-space at -1.2 V_{RHE} in CO_2-saturated 0.1 M $KHCO_3$ for (A) Cu, (B) CuGa4, (C) CuGa17 and (D) CuGa37 NPs.
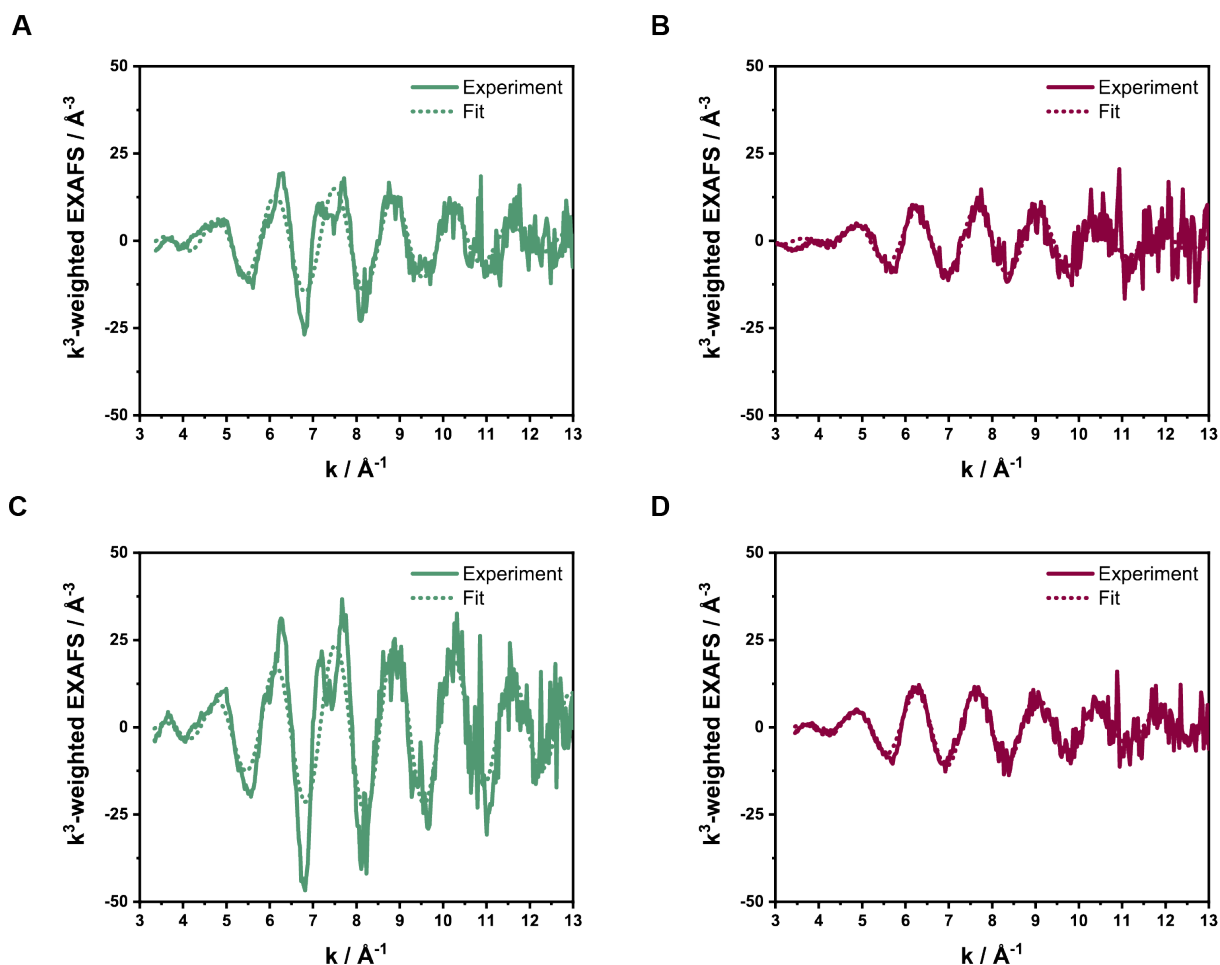
Figure S23. Experimental and fitted Ga K-edge EXAFS profiles in k-space at (A, B) ocp and (C, D) at -1.2 V_{RHE} in CO_2-saturated 0.1 M $KHCO_3$ for (A, C) CuGa17 and (B, D) CuGa37 NPs.

In all cases the range in k space fitted was $3 \leq k\,(\text{Å}^{-1}) \leq 13$. The AFAC value (see **Methods**), extracted from analysis of a copper foil, was 0.9. The approximate ranges for N1 and DWF are derived from the given correlation maps whereas, the values given for d (Å) and R% are derived from the best fit obtained through conventional analysis. In the case of d these individual values should be regarded as having an at best error of ca. 1.5 – 2 % of the stated value. However, it is considered that the correlation maps yield a more precise and insightful indication of the likely errors involved, whether or not any changes between ocp and at *operando* conditions should be considered as significant, and if so what their likely sources may be.
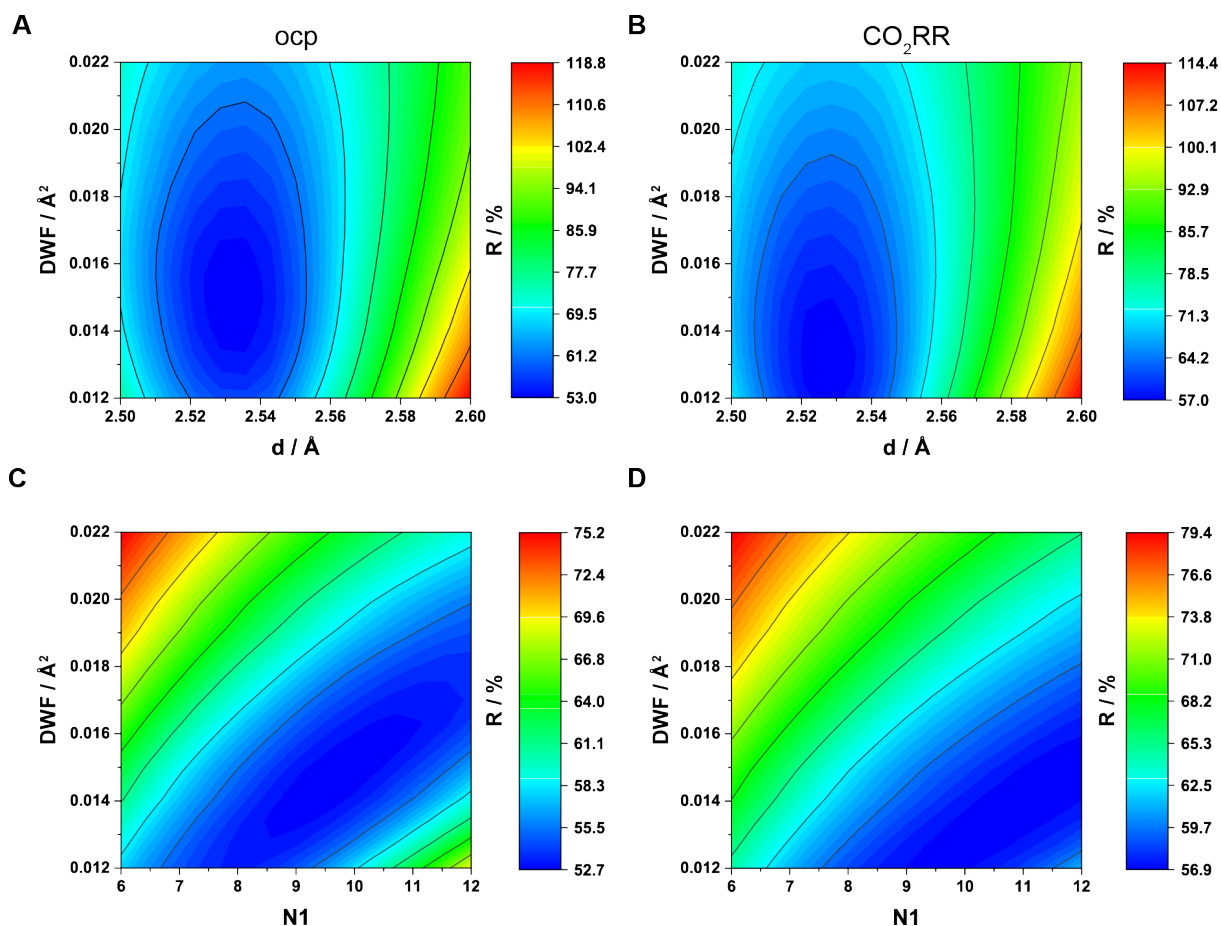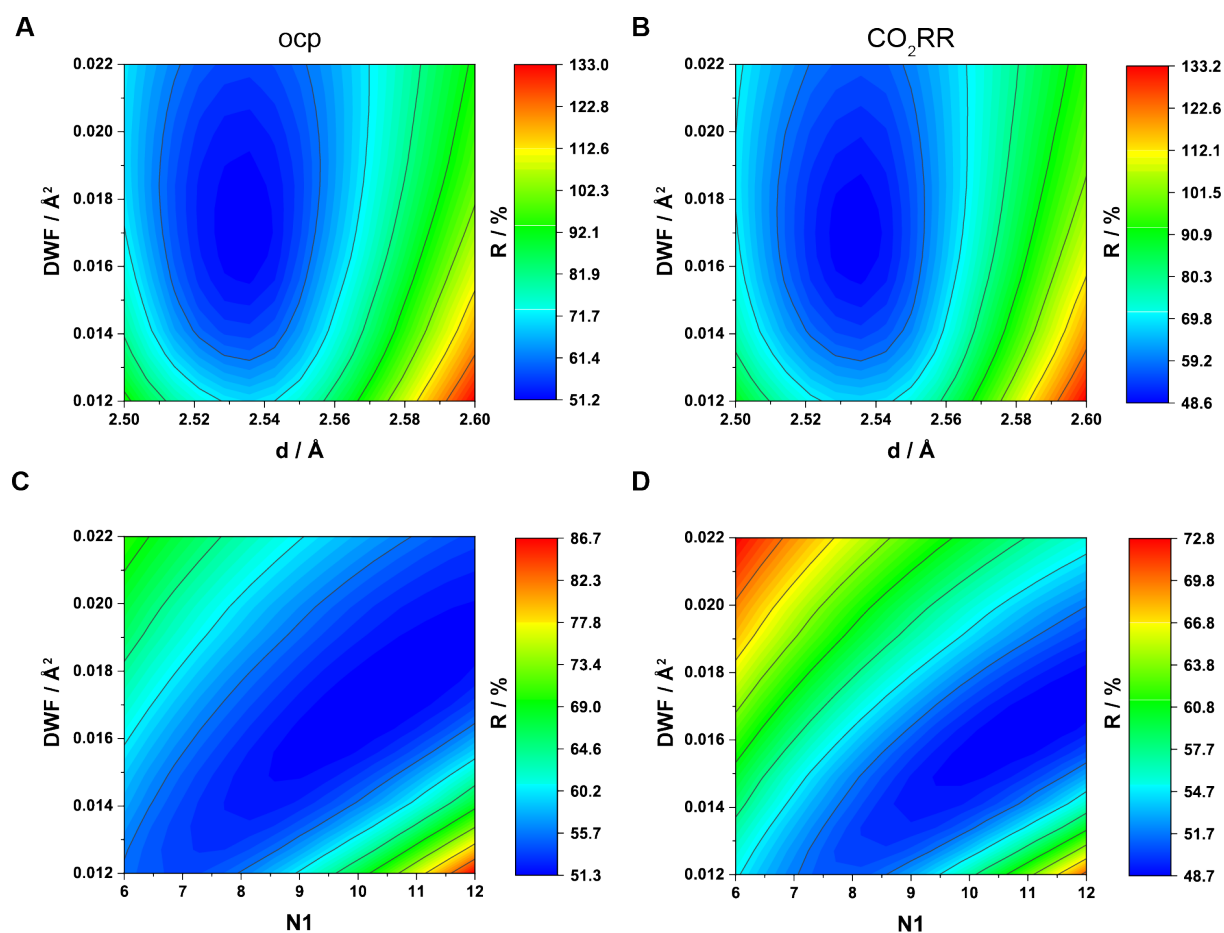
Figure S24. Contour maps (most probable values in blue) of the Debye-Waller factor (DFW, Å^2) *vs.* first-neighbor (A, B) interatomic distance (d, Å^2) and (C, D) coordination number (N1) at (A, C) ocp and (B, D) -1.2 V$_{RHE}$ in CO$_2$-saturated 0.1 M KHCO$_3$ for Cu K-edge in Cu NPs.

For the Cu sample, the correlations given above indicate the the application of CO$_2$RR has two significant effects. In the above given maps a significant downward shift in the most likely values of the DW factor can be observed. This observation indicates that a primary affect of CO$_2$RR is to increase the overall order displayed by the Cu.

At the same time, these maps show that the likely value of the coodination number shifts slightly toward higher net values. This finding can have two sources. The first is the removal of the Cu$_2$O layer initially present and the incorporation of that Cu into the majority metallic component. This phenomenon too could also reduce the overall level of disorder implied to be present from the viewpoint of the Cu K-edge. The second possibility, in some ways a corollary of this reductive process, is that the net size of the particles increases. However, given the functional form of the relationship between particle size/atomicity,[12] the likely range of values of N1 as indicated by the maps, and recalling that the starting nanoparticles are of the order of

50 nm in diameter, we cannot state this with any certainty. Moreover, the microscopy from this sample does not suggest increase in size. Thus, we conclude that the dominant source of the observed shifts is related to the reduction of any Cu_2O initally present leading to a higher net order in the reduced copper phase that remains post CO2RR

Figure S25. Contour maps (most probable values in blue) of the Debye-Waller factor (DFW, $Å^2$) *vs.* first-neighbor (A, B) interatomic distance (d, $Å^2$) and (C, D) coordination number (N1) at (A, C) ocp and (B, D) -1.2 V_{RHE} in CO_2-saturated 0.1 M $KHCO_3$ for Cu K-edge in CuGa4 NPs.

The CuGa4 system shows a decisive narrowing and downward shift (in DWF) of the correlation between N1 and the disorder parameter but little evidence for any significant shifting of the range of most likely N1 values. Again one source of this observation is likely to be the removal of any oxide layer initally present, but it could also be an enhanced order within the crystallites themselves. In this case the microscopy yields no significant change in the size distribution post CO2RR.
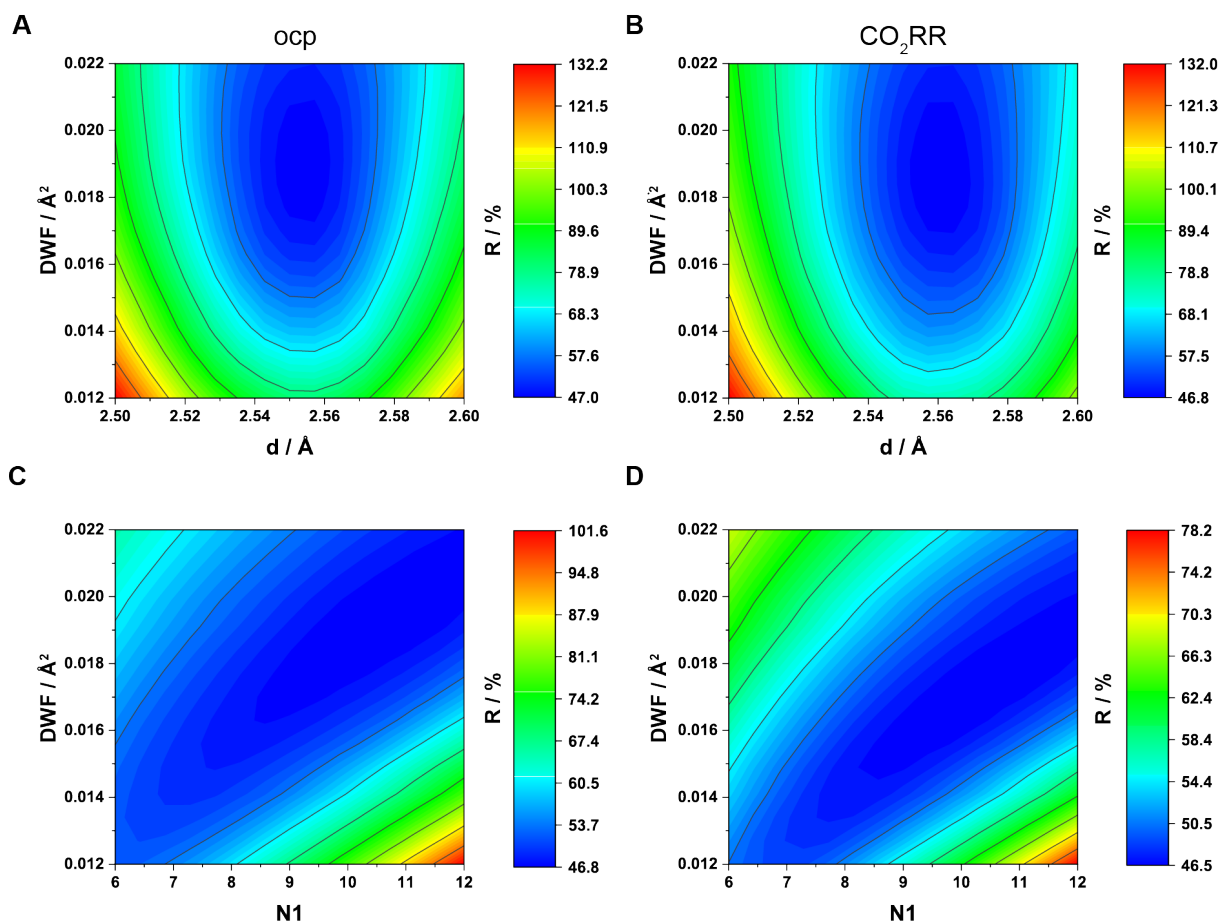
Figure S26. Contour maps (most probable values in blue) of the Debye-Waller factor (DFW, Å^2) *vs.* first-neighbor (A, B) interatomic distance (d, Å^2) and (C, D) coordination number (N1) at (A, C) ocp and (B, D) -1.2 V_{RHE} in CO_2-saturated 0.1 M $KHCO_3$ for Cu K-edge in CuGa17 NPs.

In CuGa17, firstly we see that the 1st shell interatomic distance increases relative to the previous two cases. This change is expected on the basis of the significantly higher level of Ga and the lattice expansion resulting from its incorporation into the *fcc* Cu lattice.

Furthermore, the application of CO_2RR operation conditions induces a small, but likely significant expansion of the 1st shell fcc interatomic distance (from ca. 2.55 to ca 2.56). Formally speaking, this shift is very small in term of the percentage change on overall bond length, and below that one might normally associate with the error connected to the phase of the EXAFS oscillations. However, when considered via the correlation map, this expansion appears to be likely. While small, the source of such a change might be a change in the distribution of Ga between the surface of the sample and the bulk, and is suggestive of a net migration of some Ga into the bulk of the particles as a result of CO_2RR

Concomitant with this, we again observe that the correlation between N1 and DWF narrows and shifts to slightly lower values of DWF, again indicating that the net order of the system, as viewed from the perspective of the Cu K-edge, has increased.
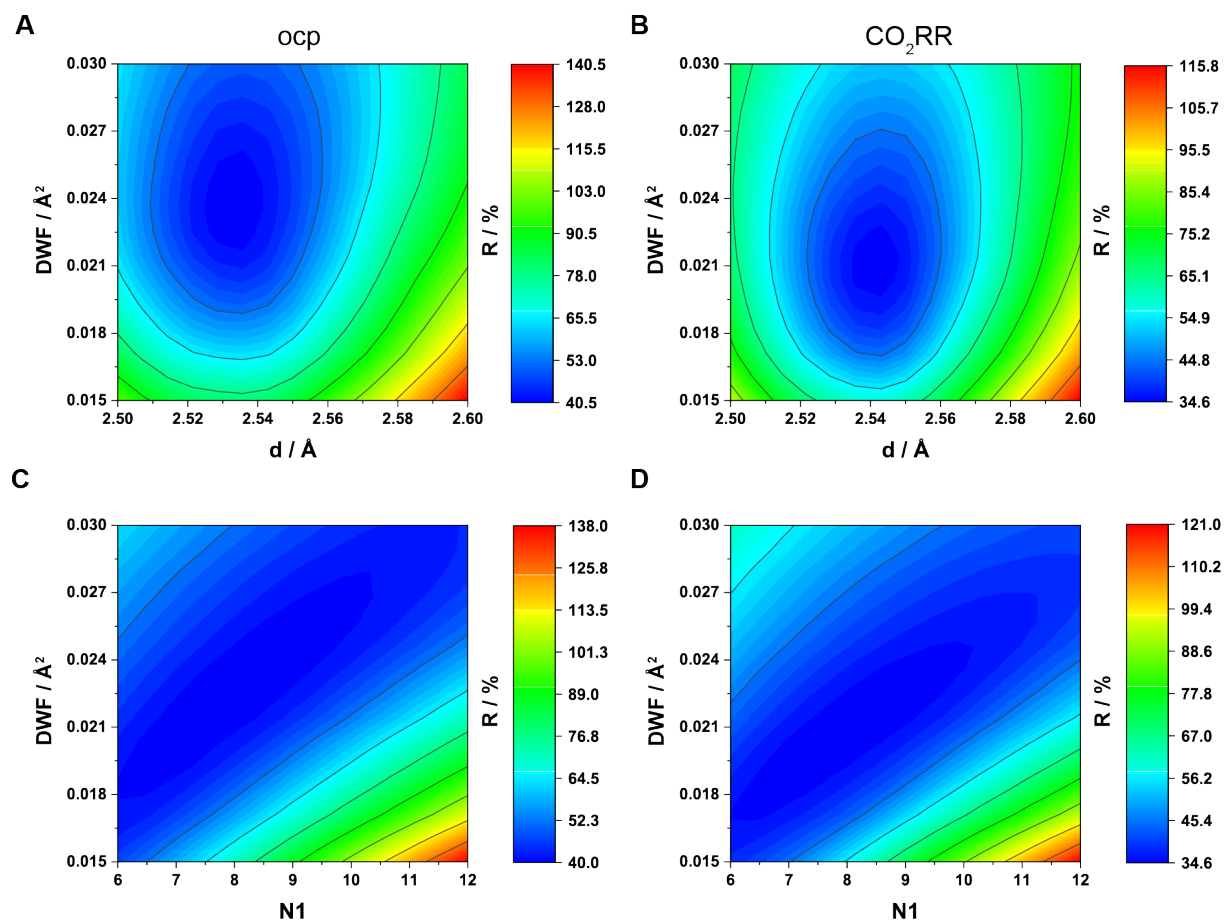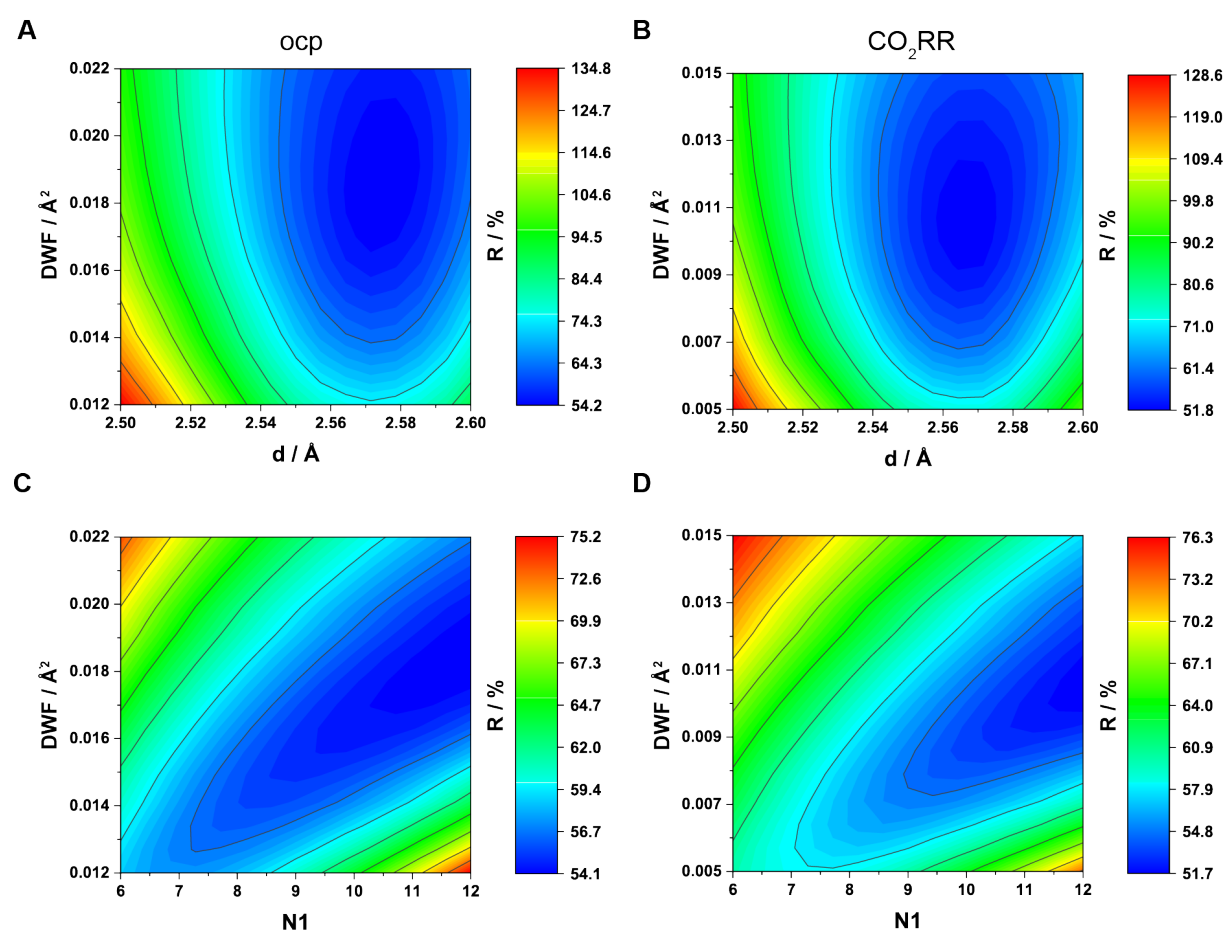

Figure S27. Contour maps (most probable values in blue) of the Debye-Waller factor (DFW, Å^2) *vs.* first-neighbor (A, B) interatomic distance (d, Å^2) and (C, D) coordination number (N1) at (A, C) ocp and (B, D) -1.2 V$_{RHE}$ in CO$_2$-saturated 0.1 M KHCO$_3$ for Cu K-edge in CuGa37 NPs.

A similar story emerges for CuGa37. However, we are no longer dealing with an fcc structure in this case but with a lower symmetry phase ($P\bar{4}3m$). Thus, the absolute values of DWF associated with this system are much higher than those returned for any of the *fcc* systems.

The application of CO$_2$RR operation conditions results in a small shift to higher 1st shell interatomic distances whilst, at the same time, narrowing and shifting DWF to lower values with no evidence for any significant shift in the most likely values of N1. A net migration of Ga into the bulk of the crystallites (again no evidence for significant changes in particle sizes

by microscopy) is deemed the most likely cause of these effects. This conclusion is in line with the Ga K-edge EXAFS data (vide infra) and the STEM-EDXS elemental mapping and line profiles shown in **Figure 5**.
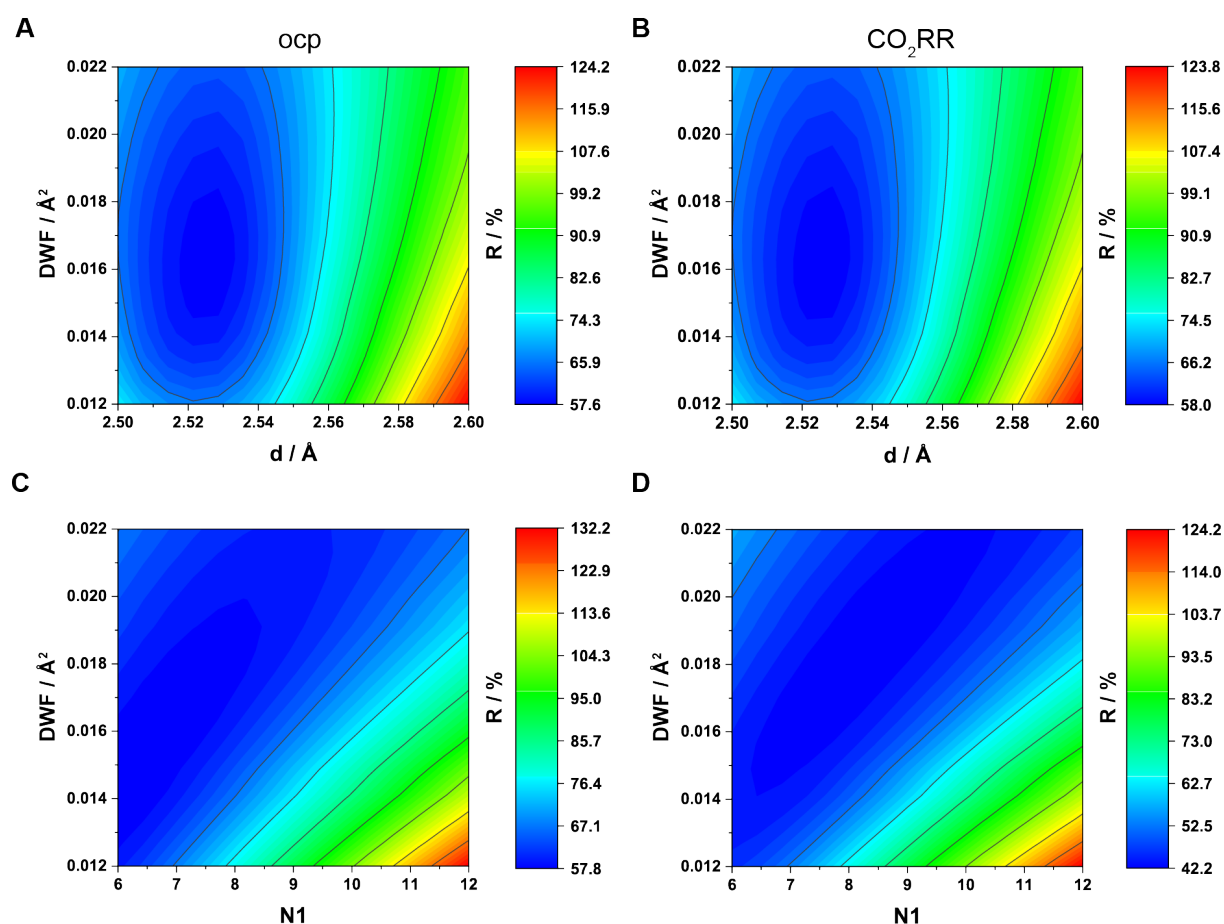

Figure S28. Contour maps (most probable values in blue) of the Debye-Waller factor (DFW, $Å^2$) *vs.* first-neighbor (A, B) interatomic distance (d, $Å^2$) and (C, D) coordination number (N1) at (A, C) ocp and (B, D) -1.2 V_{RHE} in CO_2-saturated 0.1 M $KHCO_3$ for Ga K-edge in CuGa17 NPs. Please, note the DFW scale difference between (A, C) (ocp) and (B, D) (-1.2 V_{RHE}) panels.

In two cases, CuGa17 and CuGa37, the EXAFS from the Ga K-edge was also obtained and analysed. For CuGa17 (above, **Figure S28**) the view of the system, and how it changes as a result of CO_2RR, from the perspective of the Ga, results in a variety of differences compared to the view obtained from the Cu K-edge.

Firstly, the Ga K-edge EXAFS appears to report a significantly larger 1st shell fcc interatomic difference (over 2.57 Å compared to ca. 2.54 Å), suggesting that, on average, the Ga resides within a locally expanded *fcc* structure which is not significantly perturbed by CO_2RR (in terms of d / Å or indeed DWF). Therefore, in this case, the net order around the Ga

appears not to be affected by the catalysis. Furthermore, a signficant shift (towards higher values of N1) appear in the 1st shell *fcc* coordination number while the overall order, as viewed from the perspective of the Ga, is stable. This change in the N1/DWF correlation yields strong evidence for what suggested from the Cu K-edge; that is a net migration of Ga into the more highly coordinated interior of the NPs resulting from the CO_2RR, which is again commensurate with the observations made (for CuGa37) using microscopy in **Figure 5** and **Figure S12**.

Figure S29. Contour maps (most probable values in blue) of the Debye-Waller factor (DFW, $Å^2$) *vs.* first-neighbor (A, B) interatomic distance (d, $Å^2$) and (C, D) coordination number (N1) at (A, C) ocp and (B, D) -1.2 V_{RHE} in CO_2-saturated 0.1 M $KHCO_3$ for Ga K-edge in CuGa37 NPs.

A similar story emerges from the Ga K-edge analysis of the CuGa37 system, although here, within the non-*fcc* ($P\bar{4}3m$) structure. As with CuGa17, the overall structural order of the system appears more robust toward CO_2RR. And although less marked than the changes for CuGa17, maps C and D also suggest a shift in N1 to higher values post CO_2RR and with it that a net migration of Ga into the NPs has resulted from the electrocatalysis (via à vis **Figure 5**).
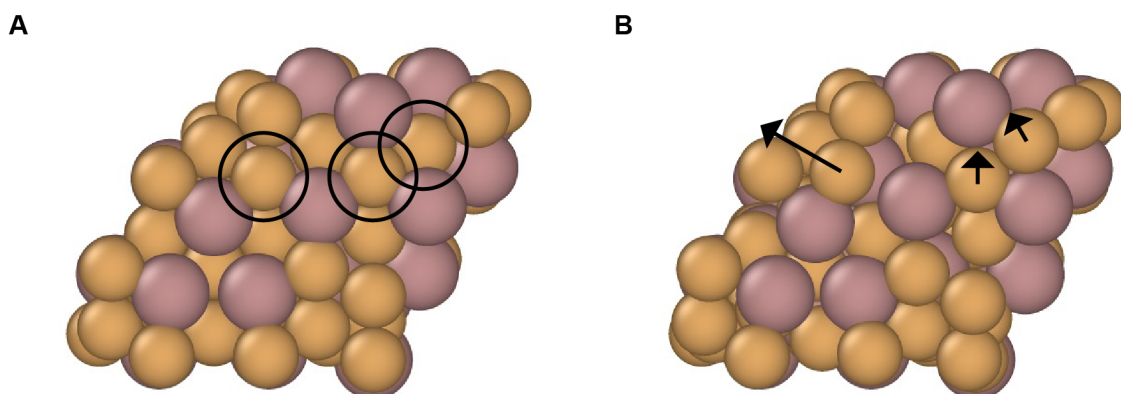
Figure S30. Molecular dynamics simulations representing the atomic arrangement for the CuGa37 surface at (A) steady conditions and (B) after 1 ps of dynamics at 900 K. The Cu atoms which appear on the surface are marked by the circles, and the arrows indicate the displacement direction. Under the same simulations conditions, Cu, CuGa4 and CuGa17 do no undergo changes. Notably, the reconstruction results in Cu atoms popping on the surface, which comes in line with STEM-EDXS line scan after 4 h of CO_2RR (**Figure 5**).

Table S2. ICP-MS measurements of Cu and CuGa NP electrodes after 5 min immersion in CO_2-saturated 0.1 M $KHCO_3$ at ocp.

Sample name	Ga, ng/ml	Cu, ng/ml
Cu	-	45
CuGa4	25	47
CuGa17	86	19
CuGa37	163	-
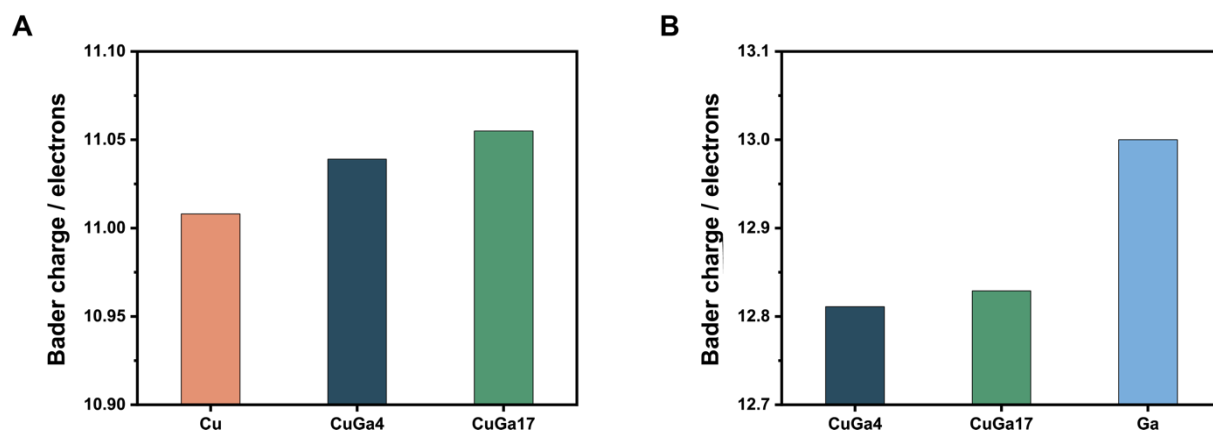
Figure S31. Bader charge calculation results for (A) Cu atoms and (B) Ga atoms in Cu and CuGa alloys. Expected values for the Bader charge of pure Cu and Ga based on the Periodic Table are 11 and 13 electrons, respectively. To avoid misrepresentation, CuGa37 was not considered to keep only the *fcc* structures, where all crystal lattice positions are equivalent to each other.

REFERENCES

(1)   Sebastián-Pascual, P.; Escudero-Escribano, M. Surface Characterization of Copper Electrocatalysts by Lead Underpotential Deposition. *J. Electroanal. Chem.* **2021**, *896*, 115446.

(2)   Plaza-Mayoral, E.; Sebastián-Pascual, P.; Dalby, K. N.; Jensen, K. D.; Chorkendorff, I.; Falsig, H.; Escudero-Escribano, M. Preparation of High Surface Area Cu-Au Bimetallic Nanostructured Materials by Co-electrodeposition in a Deep Eutectic Solvent. *Electrochim. Acta* **2021**, *398*, 139309.

(3)   Figueroa, S. J. A.; Prestipino, C. PrestoPronto: A Code Devoted to Handling Large Data Sets. *J. Phys. Conf. Ser.* **2016**, *712*, 012012.

(4)   Binsted, N. EXCURV98, CCLRC Daresbury Laboratory Computer Program. CCLRC Daresbury Laboratory: Daresbury 1998.

(5)   Hutter, J.; Iannuzzi, M.; Schiffmann, F.; Vandevondele, J. Cp2k: Atomistic Simulations of Condensed Matter Systems. *Wiley Interdiscip. Rev. Comput. Mol. Sci.* **2014**, *4*, 15–25.

(6)   VandeVondele, J.; Hutter, J. Gaussian Basis Sets for Accurate Calculations on Molecular Systems in Gas and Condensed Phases. *J. Chem. Phys.* **2007**, *127*, 114105.

(7)   Krack, M. Pseudopotentials for H to Kr Optimized for Gradient-Corrected Exchange-Correlation Functionals. *Theor. Chem. Accounts 2005 1141* **2005**, *114*, 145–152.

(8)   Henkelman, G.; Arnaldsson, A.; Jónsson, H. A Fast and Robust Algorithm for Bader Decomposition of Charge Density. *Comput. Mater. Sci.* **2006**, *36*, 354–360.

(9)   Yu, L.; Akolkar, R. Lead Underpotential Deposition for the Surface Characterization of Silver Ad-Atom Modified Gold Electrocatalysts for Glucose Oxidation. *J. Electroanal. Chem.* **2017**, *792*, 61–65.

(10)   Okatenko, V.; Castilla-Amorós, L.; Stoian, D. C.; Vávra, J.; Loiudice, A.; Buonsanti, R. The Native Oxide Skin of Liquid Metal Ga Nanoparticles Prevents Their Rapid Coalescence during Electrocatalysis. *J. Am. Chem. Soc.* **2022**, *144*, 10053–10063.

(11)   Hori, Y.; Wakebe, H.; Tsukamoto, T.; Koga, O. Electrocatalytic Process of CO Selectivity in Electrochemical Reduction of CO_2 at Metal Electrodes in Aqueous Media. *Electrochim. Acta* **1994**, *39*, 1833–1839.

(12)   Jentys, A. Estimation of Mean Size and Shape of Small Metal Particles by EXAFS. *Phys. Chem. Chem. Phys.* **1999**, *1*, 4059–4063.